Robert Zacharias, BSc

Development and Characterisation of Noble Metal Catalysts for the Direct Borohydride Fuel Cell

MASTERARBEIT

zur Erlangung des akademischen Grades

Master of Science

Masterstudium Chemie

eingereicht an der

Technischen Universität Graz

Betreuer

Assoc.Prof. Dipl.-Ing. Dr. Viktor Hacker

Institut für Chemische Verfahrenstechnik und Umwelttechnik

Graz, März 2016

Statutory Declaration

I declare that I have authored this thesis independently, that I have not used other than the declared sources / resources, and that I have explicitly marked all material which has been quoted either literally or by content from the used sources.

…… ……..

Date Signature

Abstract

The goal of this work was the development and characterisation of carbon supported nanoscale noble metal electrocatalysts for the direct borohydride fuel cell in a mixed electrolyte approach. Platinum, ruthenium, palladium, rhodium and gold nanoparticles on carbon support were synthesised and different characterisation methods were applied to obtain structural and electrochemical information.

The instant-reduction method and the polyol-method were used for synthesising the catalyst samples. Scanning electron microscopy images were taken and X-ray diffraction analysis was executed in order to determine structural information of the nanoparticles.

The main part of the experiments consisted of applying electrochemical ex-situ and in-situ methods. Cyclic voltammetry and rotating disk electrode experiments were used for the ex-situ characterisation of the anode catalyst and to find a borohydride tolerant cathode catalyst for the oxygen reduction reaction.

In-situ analysis involved recording polarisation curves in a mixed electrolyte direct borohydride fuel cell with an in-house synthesised MnO_2/C cathode to determine the cell performance in dependence of the anode catalyst. Additionally the developed hydrogen was quantified during polarisation with an electrochemical detection cell to measure the hydrolysis activity in dependence of the cell voltage.

Kurzfassung

Das Ziel dieser Arbeit war die Entwicklung und Charakterisierung von Edelmetall Elektrokatalysatoren auf einem Trägermaterial aus Kohlenstoff für den Einsatz in der Direkt Borhydrid Brennstoffzelle in einer „mixed electrolyte“ Ausführung. Es wurden Platin, Ruthenium, Palladium, Rhodium und Gold Katalysator-Nanopartikel auf Kohlenstoff abgeschieden und untersucht um strukturelle und elektrochemische Informationen zu erhalten.

Zur Synthese der Katalysator-Proben wurden die „Instant-Reduction“-Methode und die Polyol Methode herangezogen. Rasterelektronenmikroskopie und Röntgenbeugung wurden verwendet um strukturelle Informationen über die Proben zu erhalten.

Der Großteil der Charakterisierung umfasste die Anwendung von elektrochemischen ex-situ und in-situ Messmethoden. Cyclovoltammetrie und Rotating Disk Electrode Experimente wurden für die ex-situ Charakterisierung der Anodenkatalysatoren verwendet und auch zur Untersuchung von Borhydrid toleranten Kathodenkatalysatoren für die Sauerstoffreduktionsreaktion.

Die in-situ Messungen der entwickelten Katalysatorproben bestanden aus der Aufzeichnung von Polarisationskurven in einer Direkt Borhydrid Brennstoffzelle in „mixed electrolyte“ Ausführung mit einer MnO_2/C Kathode. Zusätzlich erfolgte die quantitative Bestimmung von Wasserstoff, der während der Polarisation gebildet wurde, mit einer elektrochemischen Detektionszelle.

Danksagung

An dieser Stelle möchte ich mich bei all jenen bedanken, die mich während der Anfertigung dieser Masterarbeit unterstützt und motiviert haben.

Zuerst gebührt mein Dank Prof. Dr. Viktor Hacker und DI Christoph Grimmer, die mir die Möglichkeit gaben meine Masterarbeit zu verfassen und mir immer hilfreich zur Seite standen. Auch möchte ich mich bei der Firma Proionic für die großzügige finanzielle Unterstützung bedanken.

Dankbarkeit gebührt auch allen KollegInnen in der Arbeitsgruppe des Labors für Brennstoffzellensysteme, die mich durch Ratschläge, praktische Hilfestellungen und abseits der Arbeit unterstützt haben.

Ebenfalls möchte ich mich bei meinen Kommilitonen Stefan, Manuel, Mathias und Martin bedanken, die mir mit viel Geduld, Interesse und Hilfsbereitschaft in der Lerngruppe zur Seite standen.

All meinen Freunden, meinem Bruder Martin und meiner Freundin Merit danke ich für den starken Rückhalt und Verständnis mir gegenüber.

Ganz besonders möchte ich mich bei meinen Eltern bedanken, die mir mein Studium durch ihre Unterstützung ermöglicht haben und stets ein offenes Ohr für meine Sorgen hatten.

Content

1 Introduction

"Warming of the climate system is unequivocal, and since the 1950s, many of the observed changes are unprecedented over decades to millennia. The atmosphere and ocean have warmed, the amounts of snow and ice have diminished, sea level has risen, and the concentrations of greenhouse gases have increased [1]**."**

This thesis starts with the initial statement in the IPCCs Contribution to the Fifth Assessment Report of the Intergovernmental Panel on Climate Change. Plenty measurements and records since the mid-19th century substantiate IPCCs statement. The working group found a "clear human influence" on the climate and also the great likeliness of human impact being the dominant cause of global warming since the 1950s (Fig. 1-1). The urgency of measures was highlighted, because the longer we wait to reduce emissions, the more expensive it will become [1].

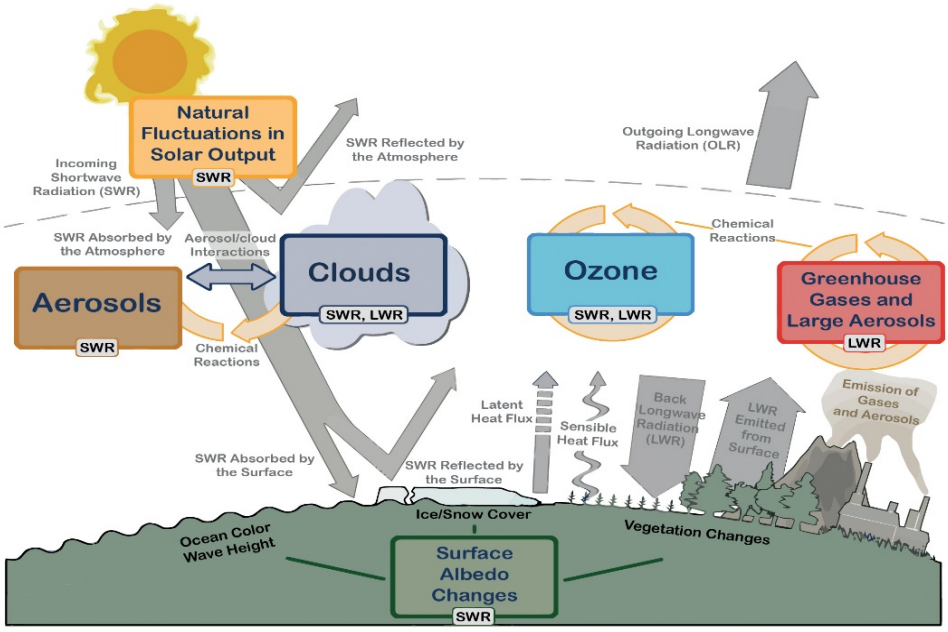

Fig. 1-1: Main drivers of climate change. The radiative balance between incoming solar shortwave radiation (SWR) and outgoing longwave radiation (OLR) is influenced by global climate drivers [2]

Finding a sustainable energy supply is a public issue since the 1970s [3]. The Suez crisis and the growing sense for the negative impact of anthropogenic emissions triggered the discussion

about alternatives to fossil energy. Reducing the global warming despite a rising energy demand is a key issue in our time [4].

In the World Energy Outlook 2015 the IEA predicts an increase of electricity generation of two percent per year, resulting in an overall growth of 70 % by 2040. In total electricity generation a fast increase in the use of renewables with its share rising to 34 % and a decrease of the fossil fuels' share from 67 % to 54 % is assumed, mainly due to governmental policies in OECD countries. Hydropower remains the largest source for renewable power generation, but wind power and photovoltaics are assumed to grow rapidly as well [5].

Especially solar- and wind power involve the challenge of time-related, geographical and weather-depending fluctuations. Therefore they are not tailored to suit the user needs. Thus it is required to extend the electrical supply network on the one hand and to implement large scale electricity storage systems with long-term stability on the other hand.

To store electricity, it has to be transformed into other forms of energy. Chemical energy storage is a very attractive technological option with high energy densities. Especially hydrogen, as presented in the framework of a clean energy economy could act as ideal storage medium (Fig. 1-2). The transformed and stored electrical energy can be recovered with low emissions and with high efficiencies by various types of hydrogen fuel cells [4].

Fig. 1-2: Factors of an economy based on hydrogen [6]

A promising example for chemical hydrogen storage is sodium borohydride. It offers the advantages of long-time stability in liquid state, easy release reaction at ambient temperature and safe handling due to low toxicity and no flammability. By exchanging the cation, the capacity can be extended. The borohydride anion provides in addition the possibility of direct energy transformation in direct borohydride fuel cells, achieving a high reversible cell voltage of 1.64 V.

2 Theory

2.1 Hydrogen Storage

The sustainable production of hydrogen involves a high number of decentralised production sites, for instance the reforming of biomass. This means that the place of production and the place of consumption will often be far apart, in this regard efficient hydrogen transport and storage technologies are required. The most common hydrogen storage is the pressurised form up to 70 MPa (700 bar) depending on the application. Besides the cost issues due to energy consumption for compression and the new infrastructure for dealing with flammable pressurised gases, this technique also requires high safety precautions.

Several alternatives to the conventional hydrogen storage were investigated in the last years. A graphical overview of hydrogen storage methods is given is given in Fig. 2-1, provided by the U.S. Department of Energy. Material based storages – in other words chemical storages are very attractive due to their high storage density. Among them, metal hydrides like $NaBH_4$, liquid organic compounds and chemical hydrides are important approaches [7–9].

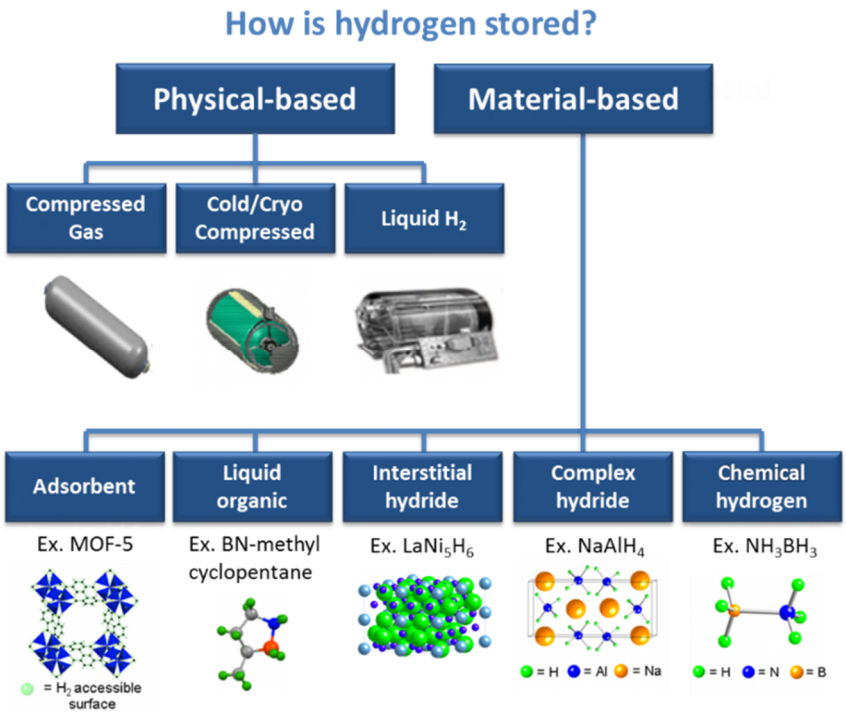

Fig. 2-1: Overview of hydrogen storage techniques [10]

2.2 Fuel Cells

Fuel cells are electrochemical devices that convert chemical energy into electricity, without heat cycle [11]. This technology is a promising alternative to heat engines due to their high efficiency while releasing low amounts of emissions [12]. Fuel cells are developed for a number of applications e.g. for mobility applications or for the utility industries [3].

The storage of the energy carrier - the fuel - separately categorises fuel cells as tertiary electrochemical cells. Primary and secondary cells have the drawback of an operation time limited to the cell's capacity that is directly linked to the size and weight. The operation time of fuel cells does not depend on the size of the cell, since energy is converted as long fuel and oxidant are supplied. So fuel cells combine the benefit of combustion engines with the direct energy conversion of electrochemical cells.

Fuel cell types (Fig. 2-2) can be distinguished in terms of their operating conditions in high-, mid- and low temperature FCs, whereas the main categorisation is made by their type of electrolyte [13]:

- Proton-exchange membrane fuel cells (PEMFCs)
- Alkaline fuel cells (AFCs)
- Solid oxide fuel cells (SOFCs)
- Phosphoric acid fuel cells (PACFs)
- Molten carbonate fuel cells (MCFCs)

Direct liquid fuel cells are usually named after their fuel, i.e. the direct methanol fuel cell (DMFC) or the direct borohydride fuel cell.

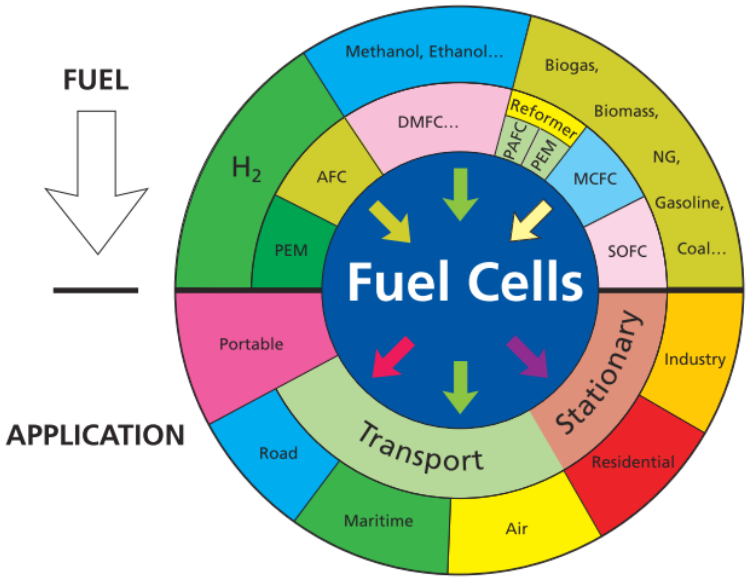

Fig. 2-2 Fuel cells and their applications [14]

The first accomplishments of fuel cells in practical use were made with AFCs using hydrogen as fuel. In this context the AFC driven Austin A40, built by Prof. Kordesch and the NASAs "Apollo program" should be mentioned. After its first success the alkaline approach fell back behind the acidic one, mainly due to the invention of proton exchange membranes and the PEMFC, which is nowadays the most established type of fuel cell [15].

However, AFCs have the advantage of higher cell voltages due to the faster kinetics at the cathode and the possibility of using cheaper non-noble metal catalysts. The recent progress of alkaline membranes has promoted the research in this field of fuel cells again [16].

2.3 Efficiency of Fuel Cells

As mentioned above, the key benefit of a fuel cell is its high theoretical electrical efficiency that is not limited by the Carnot cycle. The ideal electrical efficiency can be described as relation between the Gibbs free energy of the reaction ΔG and the Enthalpy change ΔH of the cell reaction. η_{th} is the theoretical or reversible efficiency being the maximal possible value limited by the restrictions of thermodynamics. T is the absolute temperature and ΔS the entropy change for the reaction.

$$\eta_{th} = \frac{\Delta G^0}{\Delta H^0} = \frac{\Delta H^0 - T\Delta S^0}{\Delta H^0} \qquad (1)$$

Most cell reactions have a negative entropy change; therefore the theoretical efficiency is lower than 100 %. However, there are reactions with a positive entropy change and therefore the reversible efficiency becomes higher than 100 %. These reactions withdraw heat from the environment at constant reaction temperature. An example is the formic acid oxidation, with a theoretical efficiency of 106 % at 25 °C. The most widespread hydrogen fuel cell has a theoretical efficiency of 83 % at 25 °C with liquid water as reaction product [17].

The electrical energy needed to move the released electrons of one mole reacted fuel is -zFE, where F is the charge of one mole electrons (the Faraday constant), z is the amount of exchanged electrons and E is the cell voltage. In the theoretical case of a reversible system with E^0 being the reversible cell voltage, this work is equal to the Gibbs free energy of the reaction.

$$\Delta G^0 = -zFE^0 \qquad (2)$$

The high theoretical efficiencies of fuel cells are not possible in the practical use because of irreversible energy losses due to different phenomena. These losses are called “overpotentials”, “irreversibles” or “voltage drop”, all meaning the same effects. The non-utilizable voltage is transformed into heat and can be depicted in the so-called polarisation curve.

2.4 Polarisation Curves

The theoretical maximum open cell voltage (OCV) in a hydrogen fuel cell is 1.23 V at 25 °C. However, this voltage is not observed in real conditions, whereas OCVs of less than 1.1 V are realistic. At low current densities the voltage decreases sharply, followed by a linear voltage drop over a long range and a sharp voltage drop at high current densities. Fig. 2-3 illustrates this typical V/I-curve for a fuel cell and shows the three kinds of overpotential, occurring at the typical current density regions.

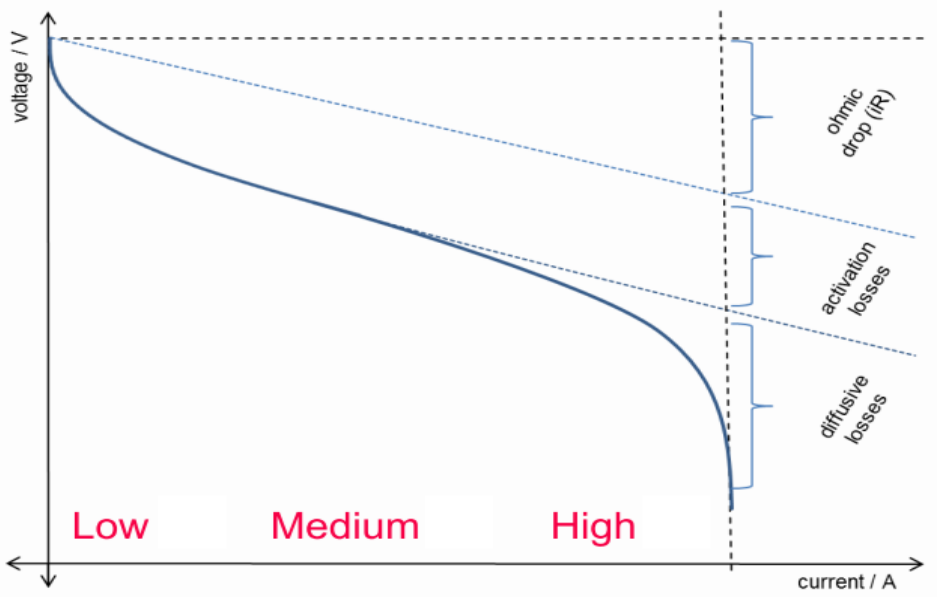

Fig. 2-3: Exemplary polarisation curve of a fuel cell, showing the three contributions to voltage drop at particular current densities [18]

1. The first region at low current densities experiences the initial energy loss and shows a non-linear behaviour, due to reaction overpotential. The curve form is described by the Butler-Volmer equation.
2. At medium current densities a linear voltage drop can be seen described by Ohm's law, owing to the internal resistance of the cell.
3. The region at high current densities is the diffusion limited region with a non-linear behaviour described by Fick's law.

2.5 Electrocatalysis

According to the International Union of Pure and Applied Chemistry (IUPAC), catalysis is a process that increases the rate of a reaction, without the alteration of the overall standard Gibbs energy change in the reaction [19]. This happens by lowering the activation energy of a reaction without consumption of the catalyst (Fig. 2-4).

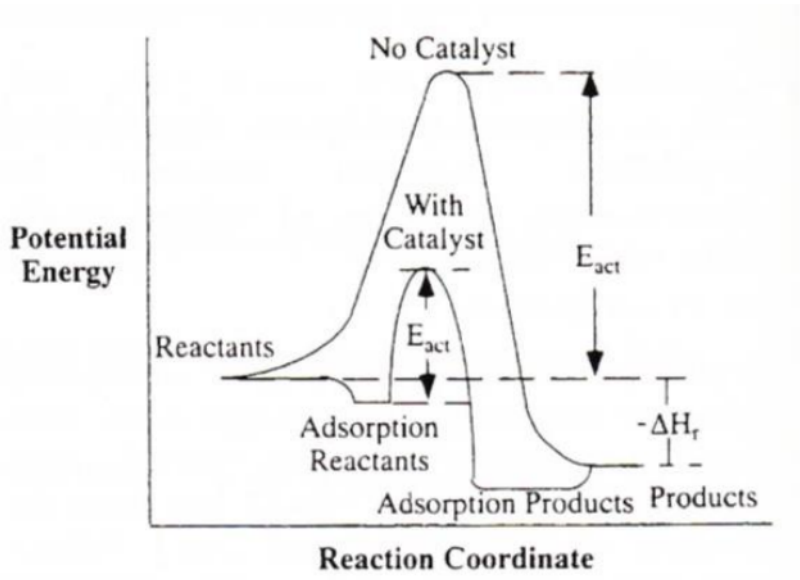

Fig. 2-4: Potential energy vs reaction coordinate of a catalysed and an uncatalysed reaction [20]

Electrocatalysis links the broad field of catalysis with electrochemistry, via enhancing the kinetics of electrochemical reactions. It is a fundamental subject in processes where interfacial charge transfer reactions have to be controlled. This shows the high importance of electrocatalyst development in areas of fuel cell-, solar fuel- and electrosynthesis research [21].

The morphology of catalysts must be adjusted to yield a high surface to volume ratio and also a good activity. As the amount of active layer correlates directly with costs, it is crucial to minimise the needed catalyst quantity. This indicates why nanoparticles on a support material are often used in heterogeneous catalysis. In case of gaseous reactants, an additional gas diffusion layer (GDL) is needed that connects the supported catalyst with the current collector [22].

2.6 Direct Borohydride Fuel Cells

Borohydride can be used in direct liquid fuel cells for the direct conversion of its chemical energy into electricity. DBFCs can achieve a high theoretical voltage of 1.64 V using O_2 as oxidising agent [23].

$$BH_4^- + 8OH^- \rightarrow BO_2^- + 6H_2O + 8e^- \quad E^0_{anode} = -1.24 \text{ V vs. SHE} \qquad (3)$$

$$O_2 + 2H_2O + 4e^- \rightarrow 4OH^- \quad E^0_{anode} = 0.40 \text{ V vs. SHE} \qquad (4)$$

$$BH_4^- + 2O_2 \rightarrow BO_2^- + 4H_2O \quad E^0_{cell} = 1.64 \text{ V vs. SHE} \qquad (5)$$

The best results for the anode reaction are achieved with Pt particles in the nm range on high surface area carbon support materials. Basically, alkaline media enable both noble and non-noble metal catalysts in the active layer.

The biggest challenge is the hydrolysis of the borohydride anion on particular catalyst materials including platinum (equation 6) [24]. This reaction leads to mechanical stress on the anode, a mixed potential with contributions of equation 3 (-1.24 V vs SHE) and equation 7 (-0.828 V vs SHE) and the cell`s open circuit voltage decreases. Liu et al. [25] discovered that the concentration of OH^- has to be at least 4.4 times higher than the borohydride concentration to enable a full eight-electron borohydride oxidation.

$$BH_4^- + 2H_2O \rightarrow BO_2^- + 4H_2 \qquad (6)$$

$$H_2 + 2OH^- \rightarrow 2H_2O + 2e^- \quad E^0_{anode} = -0.828 \text{ V vs. SHE} \qquad (7)$$

It is important to find anode catalyst materials for borohydride oxidation without activity towards hydrolysis. The addition of chemical compounds like thiourea (TU) to the borohydride fuel solution can diminish the hydrolysis reaction on platinum but also influences the borohydride oxidation [23,26].

2.7 Fuel Cell Designs of DBFC

DBFCs without a solid membrane (mixed reactant or mixed electrolyte) as well as DBFCs with membranes separating anode and cathode are investigated. The membrane approach can use either cationic or anionic membranes. Cationic membranes have the disadvantage of destabilising the borohydride solution because the pH decreases in the anodic compartment of the cell. Formation of sodium hydroxide on the cathode is another drawback, as Na^+ is transferred from the anodic to the cathodic compartment. DBFCs with anion exchange membranes do not cause these effects [27].

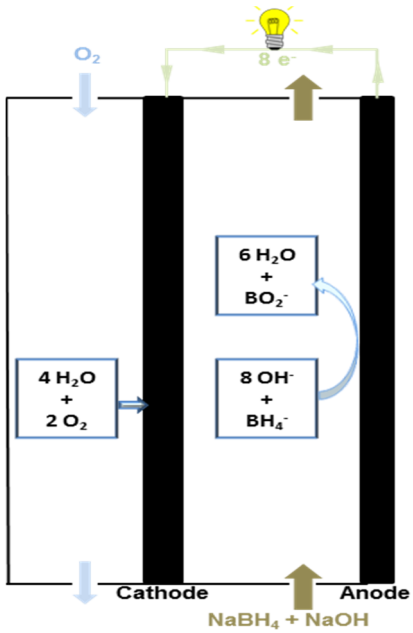

Fig. 2-5: Schematic design of DBFC – mixed electrolyte

In contrast to the majority of fuel cells the DBFC can also be operated in a membrane-less type of construction. This requires highly selective catalysts on both electrodes, since fuel and oxidant are present in the electrolyte. A mixed reagent approach can be found in literature that uses a design similar to batteries, in which the cell compartments are rolled [28,29].

Fig. 2-5 shows the schematic design of the mixed electrolyte approach for the DBFC. This design has the major advantage of the absence of oxygen at the anode, therefore only the cathode catalyst has to be highly selective. An investigation on the borohydride tolerance of Pt and Ag-MnO_2 cathode catalysts was executed at TU Graz [30].

3 Experimental

3.1 Preparation of Anode Electrocatalysts

All electrocatalysts besides Rh/C were synthesised by the instant reduction method [31]. The desired amount of Vulcan XC72R was suspended in a mixture of 2-propanol and ultrapure water for 20 minutes with an ultrasonic homogeniser. When the suspension was well-dispersed, the precursor salt was added in the appropriate amount and dissolved in 2-propanol, resulting in the metal loading of 40 wt.%.

During the Pd/C synthesis, the addition of 2.5 eq of NaCl followed by extensive sonication was necessary, due to the poor solubility of $PdCl_2$ in water. The pH of the mixture was adjusted to 9–10 with 1 M NaOH and the temperature was kept at 60 °C under continuous stirring overnight. After the addition of hydrogen or $NaBH_4$ as reducing agent the suspension was stirred for six hours at ambient temperature. The solid product was filtered, washed repeatedly with ultrapure water and dried overnight at 80 °C.

The synthesis of Rh/C was carried out with the polyol-method, using polyvinylpyrrolidone (PVP) as spacer [32,33]. Vulcan XC 72R and 0.1 eq PVP were dissolved in ethylene glycol in a round bottom flask. The mixture was heated with a heating mantle to reflux and kept there for one hour under continuous stirring. A slow heating rate of about 2 °C min^{-1} – 5 °C min^{-1} and high purity of substances are crucial. Then the polyol solution was cooled down at room temperature overnight and filtered by centrifugation. The dry Rh/C catalyst was dried at 80 °C overnight and then tempered at 200 °C for 2 hours. The temperature treatment is necessary to remove the remaining PVP molecules.

3.2 Preparation of Cathode Electrocatalysts

3.2.1 Ag-Mn_3O_4/C

An impregnation-pyrolysis method was used for this synthesis [34]. At first the precursor ($AgMnO_4$) was synthesised: equimolar solutions of $AgNO_3$ and $KMnO_4$ were mixed at 80 °C and nitric acid was added to lower the pH of the solution. The mixture was cooled down to 0 °C, to achieve precipitation of $AgMnO_4$ in form of dark blue needles. The deposit was filtered and washed with ice water.

At 40-50 °C, a proper amount of the synthesised precursor was added to a suspension of Vulcan XC72R and Black Pearls 2000 in ultrapure water. Then the suspension was treated with an ultrasonic homogeniser to achieve a homogenously dispersed colloid. The water was removed at mild conditions at 60 °C and the achieved solid was ground and temperature treated at 400 °C (inert atmosphere, heating ramp: 5 °C min^{-1}).

3.2.2 MnO_2/C

MnO_2/C was synthesised according to Wang et al. [35]. The appropriate amount of Vulcan XC72R was suspended for 20 minutes in a solution of ethanol and ultrapure water with an ultrasonic homogeniser. Then the right amount of $Mn(NO_3)_2*4H_2O$ was added, followed by homogenisation for additional 10 minutes. The homogenised reaction mixture was heated to 110 °C until all solvents were completely removed. After drying the remaining solid, underwent temperature treatment at 400 °C for two hours.

3.3 Structural and Chemical Analysis

3.3.1 Scanning Electron Microscopy (SEM)

The structure of the synthesised catalysts was analysed by scanning electron microscopy (SEM) using a Zeiss Ultra 55 device. An in-lens detector was used at 15 kV to detect secondary electrons (SE) taking images of the surface morphology at various magnifications. Additionally an angle selective backscattered electron (BSE) detector (Zeiss) was employed to show material differences.

An electron beam is accelerated to high energies between 2 and 1000 keV. This corresponds to a wavelength of 0.027-0.0009 nm. The electron beam interactions with the specimen can occur in different ways to gain diverse information by collecting specific signals. SE escape from the probe with an energy below 50 eV because of the collision with an incident electron (Fig. 3-1). Signals collected with the secondary electron detector give topographical information [36].

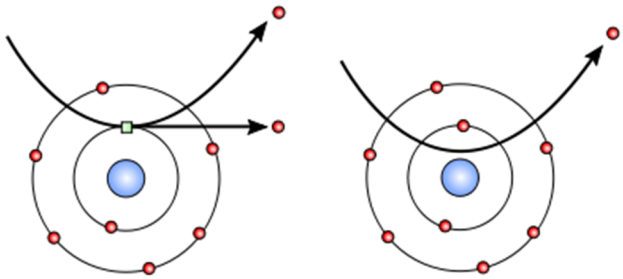

Fig. 3-1 Schematic representation of secondary electron generation (left) and back scattered electrons (right) [36]

Back scattered electrons are those beam-electrons that reach the nucleus close enough to be scattered in a large angle. They have a much lower resolution than secondary electrons because their origin from deeper layers of the specimen. Elements of higher atomic mass give a brighter contrast, so backscattered electrons deliver information about the composition of the probe. There are several more electron beam induced effects that can be used in electron microscopy, but the explanation would go beyond the scope of this thesis.

3.3.2 X-ray Powder Diffraction

The Ru catalyst was analysed with a Bruker AXS D8 Advance powder diffractometer in Bragg–Brentano geometry (40 kV, 40 mA, Cu Kα radiation (λ = 1.54178 Å)). The diffraction angles from 10 to 100°2θ were measured, with a step size of 0.025°2θ.

Starting with the crystal structure data of hexagonal metallic Ru, the Rietveld refinement was made via the PANalytical X'Pert High Score Plus software [37].

The estimation of the average primary crystallite sizes of the samples (d_{XRD}) was made in virtue of the broadening of the diffraction peaks. Therefore the Scherrer relationship was used [38]:

$$d_{XRD} = \frac{K\lambda}{\Delta(2\theta)\cos\theta} \qquad (8)$$

d_{XRD} mean crystallite dimension
K shape factor (0.9)
λ X-ray wavelength in nm
$\Delta(2\theta)$ peak broadening compared to LaB_6 standard peaks at full width at half-maximum
θ Bragg angle

3.4 Electrochemical Characterisation

All electrochemical measurements were carried out with a Reference 600 and an Interface 1000 potentiostat from Gamry instruments. The standard three-electrode configuration was used with a glassy carbon counter electrode and a reversible hydrogen electrode (RHE) as reference. All experiments were executed in a measurement cell at ambient temperature. A polished glassy carbon RDE from Pine Instruments, covered with a thin catalyst layer served as working electrode.

The desired quantity of catalyst was suspended with an ultrasonic homogeniser in a mixture of 2-propanol and ultrapure water (7:3), until a homogenous suspension was achieved. 10 µl of the fine dispersed suspension were pipetted onto the glassy carbon disk to get a catalyst loading of 28 µg cm^{-2} or 56 µg cm^{-2} for the anode catalysts and 112 µg cm^{-2} for the cathode catalysts. These loadings follow the optimised criteria, proposed by Mayrhofer et al. [39].

The catalyst suspension was dried at ambient temperature through rotation with 700 rpm, to achieve a thin and homogenous catalyst layer. 1 M NaOH made of volumetric concentrate (FIXANAL) and ultrapure water (18.2 MΩ) served as electrolyte. The concentration of BH_4^- in rotating disk electrode measurements was set to 5 mM. Levich (L) and Koutecky–Levich (KL) analyses were carried out as suggested by Treimer et al. [40].

3.4.1 Rotating Disk Electrode

The RDE method is the most widespread part of so called hydrodynamic electrochemical measurements in which a forced convection is applied to the solution. As convection during long lasting hydrostatic experiments cannot be avoided, forced convection has the advantage of well-defined motion in the solution. Steady state is reached quickly and the measurements can be made with high precision, also double-layer charging does not appear in the measurement [41].

RDE behaviour is described mathematically by the Levich and Koutecky-Levich equations. Levich equation describes the full mass-transfer dependent conditions at the RDE, giving a direct relation between the limited current, the square-root of the rotation rate and the concentration of the active species. Levich analysis involves the measurement of a series of voltammograms at different rotation speeds and plotting the current versus the square-root of

the rotation speeds to obtain the so called Levich-Plot. The Levich-equation (9) predicts a linear behaviour of the limiting current in dependence of the square-root of the rotation speed for currents, limited only by mass transportation. Via the Koutecky-Levich plot also the current in hypothetical absence of all mass transfer phenomena is considered (=kinetic limited current) and the heterogeneous rate constant (k^0) can be determined.

Levich equation:

$$i_l = 0.62\, n\, FA\, {D_R}^{2/3}\, v^{-1/6} \omega^{1/2}\, C_b \qquad (9)$$

i_l limited current
n transferred electrons
F Faraday-constant
A electrode area
D diffusion coefficient
ω rotation speed
v kinematic viscosity
C_b bulk concentration

Levich and Koutecky-Levich analysis are often used to determine the number of electrons transferred during a reaction. Linearity of the graph in the Levich plot indicates a single-step mechanism of n electrons with a large heterogeneous rate constant, whereas a bent graph in Levich plot is characteristics for a sluggish kinetics and Koutecky-Levich plot is recommended. Koutecky-Levich plot shows the reciprocal current versus the reciprocal square-root of the rotation rate[40]. Levich and Koutecky-Levich-plots are used in chapter 3.4.1.

Koutecky-Levich equation:

$$\frac{1}{i} = \frac{1}{i_l} + \frac{1}{i_k} = \frac{1}{0.62\, n\, FA\, D^{2/3}\, v^{-1/6} \omega^{1/2}\, C_b} + \frac{1}{n\, F\, A\, k_h\, C_b} \qquad (10)$$

i_l limited current
i_k kinetic limited current
n transferred electrons
F Faraday-constant
A electrode area
D diffusion coefficient
ω rotation speed
v kinematic viscosity
C_b bulk concentration
k_h heterogeneous rate constant

3.5 Preparation of Anodes

Five different anodes (Pt/C, Ru/C, Pd/C, Rh/C and Au/C) were fabricated, each containing a catalyst loading of 1 mg cm^{-2}. The preparation was done by employing a drop-coating method to soak the carbon cloth substrate with the right amount of catalyst suspension. The catalyst suspension was prepared by suspending the appropriate amount of catalyst powder with an ultrasonic homogeniser in of 1-propanol and 30 wt.% (based on the catalyst amount) FAA3 ionomer as binder. After drying at 40 °C, the electrodes were treated with 0.5 M HCl and 1 M NaOH to exchange the carbonate anions from the ionomer with hydroxide anions.

3.6 Preparation of the Cathode

The active layer of the cathode consisted of 85 % MnO_2/C (catalyst) and 15 % PTFE (binder), manufactured by a cross rolling, hot pressing method [42]. The gas diffusion layer (GDL) consisted of 55 wt. % acetylene black, 45 wt.% PTFE, with a nickel mesh as current collector. The active layer was prepared by blending the adequate amounts of catalyst and binder in a mixture of water and 2-propanol until the desired consistency was achieved. The obtained mass was cross rolled onto the GDL achieving a catalyst loading of about 40 mg cm^{-2}. The combined layers were pressed at room temperature with a pressure of 220 kg cm^{-2} to a thickness of 1.3 mm.

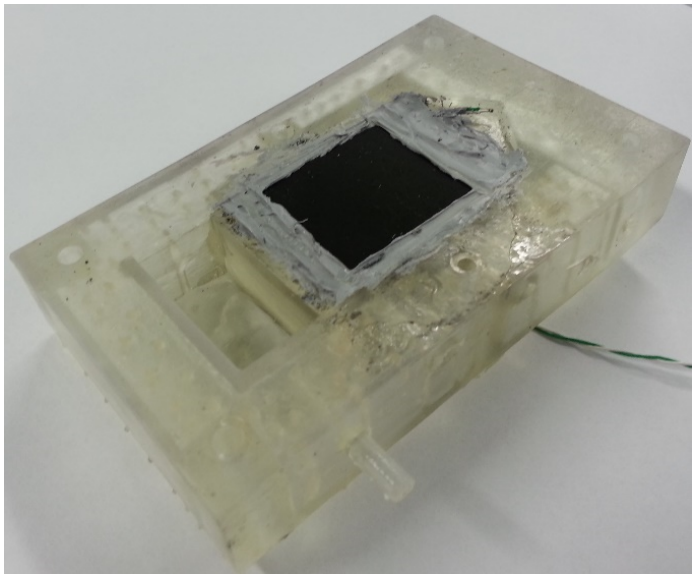

Fig. 3-2: cathode attached to the cathode holder; active layer: 85 % MnO_2, 15%PTFE

3.7 Fuel Cell Tests

The five synthesised anode catalysts were characterised in a mixed electrolyte fuel cell with an active area of 4 cm^2 versus a MnO_2 cathode. The cell design was made of a fuel inlet below the electrodes and the outlet above (see Fig. 2-5). The two anode parts were sandwiched between the current collector and the cathode. During all measurements the anode potential vs RHE was measured through a Luggin capillary, the cathode potential was calculated from the cell voltage.

1M $NaBH_4$ in 1 M NaOH and 5 mM thiourea was used as fuel/electrolyte solution and pumped through the cell with a flow rate of 10 ml min^{-1}. By the addition of thiourea to the fuel, the borohydride hydrolysis reaction should be poisoned on the catalyst surface. Pure oxygen was supplied to the cathode holder with a flow rate of 30 ml min^{-1}. All measurements were conducted both at ambient temperature and 40 °C. The polarisation curves were measured in galvanostatic mode, the current steps were held for 300 s to achieve voltage stability.

3.7.1 Measurement of Hydrogen Evolution

The hydrogen evolution in dependence of current density was measured during the record of the polarisation curves. This selective real-time H_2-quantification could be managed by passing the cells off-gas via N_2 carrier gas stream to a sensitive electrochemical hydrogen measurement cell, described by Grimmer et al. [43].

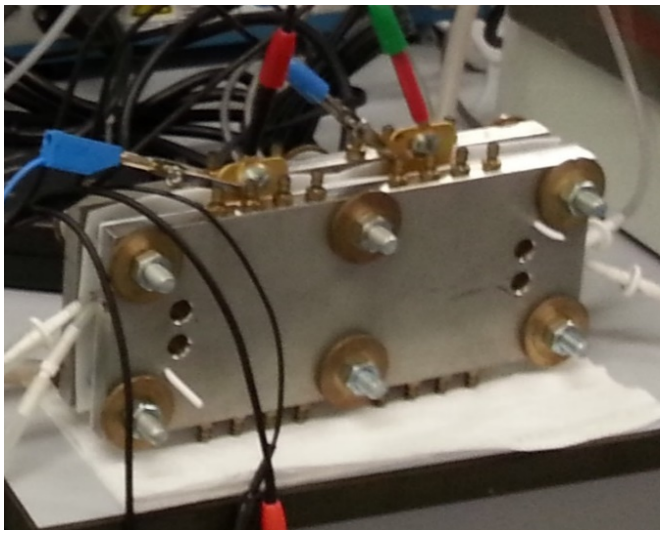

Fig. 3-3: electrochemical hydrogen detection cell

4 Results and Discussion

4.1 Structural and Chemical Analysis

4.1.1 Ru/C

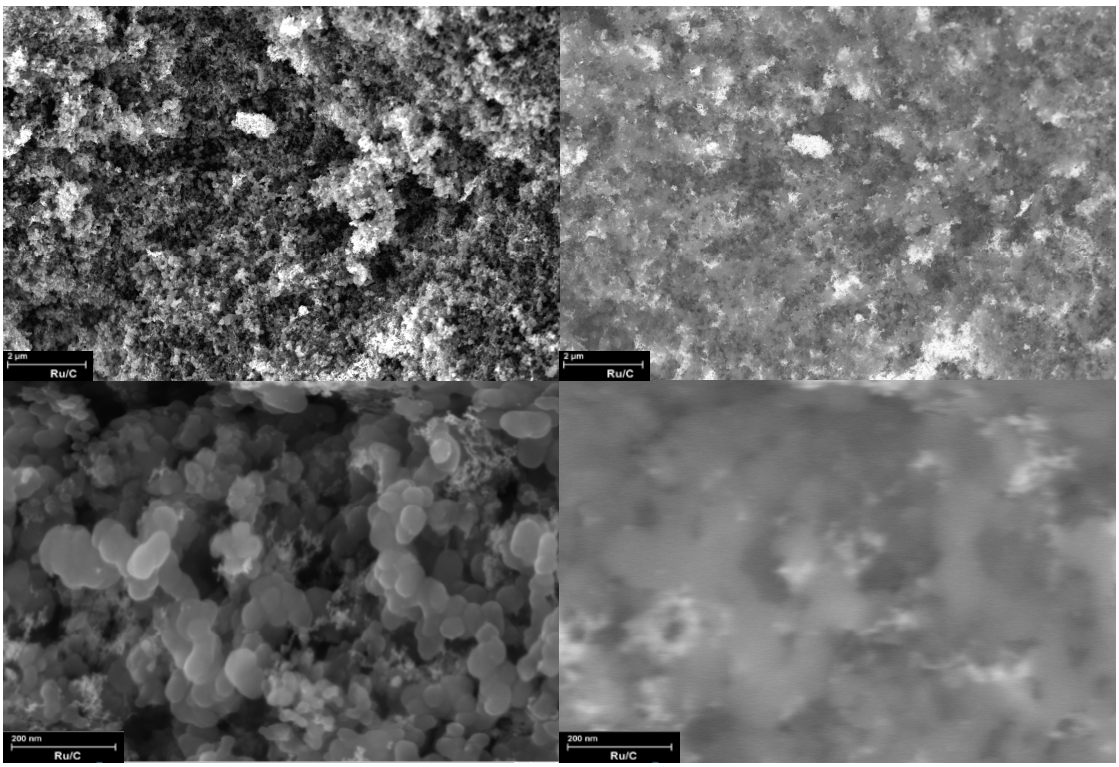

Fig. 4-1: SEM-images of the Ru/C catalyst: left column: in-lens detector images at two magnifications; right column: BSE detector, giving elemental contrast images at two magnifications

Fig. 4-1 illustrates the SEM images of the synthesized Ru/C catalyst, providing a detailed view of the electrode surface in the left images. In these figures, the spherical architecture of the carbon support can be seen. The catalyst material is agglomerated on the support material having a bigger particle size.

The image on the right shows the back scattered electron images that were taken with the BSE detector. These images show a visual representation of material contrasts and the corresponding distribution. The presence of various sized Ru agglomerates is revealed with an approximate size range from nm to µm scale.

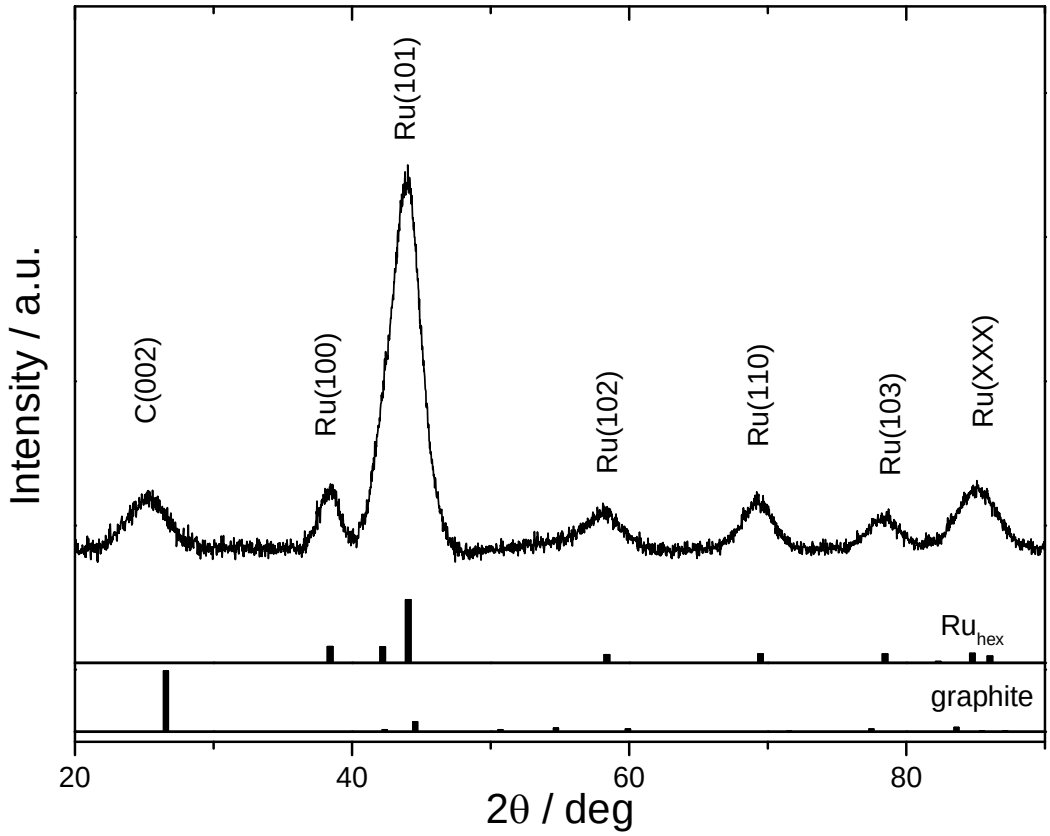

Fig. 4-2: XRD pattern of synthesised Ru/C powder [44]

Ru/C diffraction patterns can be found in Fig. 4-2. As follows from this figure, there is a good agreement of the 2θ Bragg peaks at approx. 25.6 °, 38.6 °,42.4°, 44.0 °, 58.1 °, 69.2 °, 78.5 °, 84.5° and 85.6 ° with the hexagonal reflections of C(002), Ru(010), Ru(002), Ru(011), Ru(012), Ru(110), Ru(013), Ru(112) and Ru(021), respectively [37].

In order to determine the average particle size of the Ru/C catalyst, the Scherrer equation was used [38]. The results show that the crystallite sizes are within the order of 3.0 nm. The quantification obtained by fitting the diffraction pattern indicates a Ru content of about 38 wt.%.

4.1.2 Pd/C

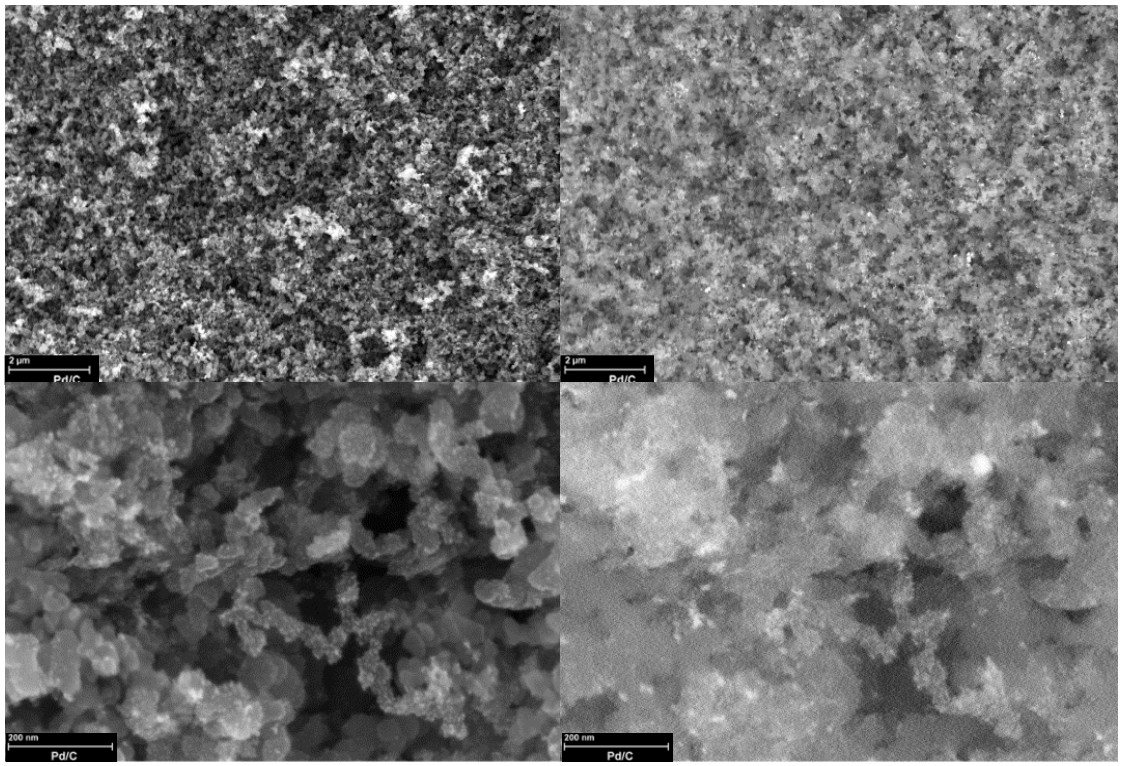

Fig. 4-3: SEM-images of the Pd/C catalyst: left column: in-lens detector images at two magnifications; right column: BSE detector, giving elemental contrast images at two magnifications

As shown in the BSE images of in the right column Pd is distributed more homogeneously on the carbon support than Ru. The carbon support's spherical structure can be seen once more. The back scattered electron images show a smaller agglomeration size of the Pd/C particles on the support material.

4.1.3 Au/C

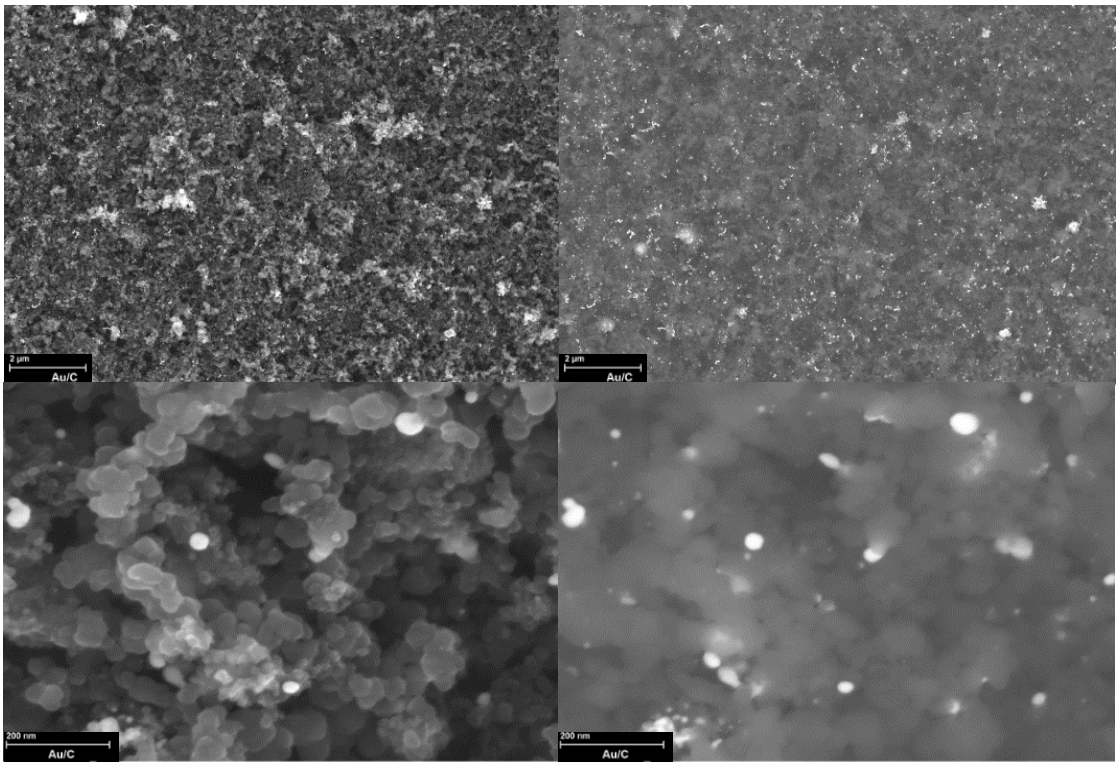

Fig. 4-4: SEM-images of the Au/C catalyst: left column: in-lens detector images at two magnifications; right column: BSE detector, giving elemental contrast images at two magnifications

The gold nanoparticles are agglomerated in spherical "islands" on the carbon support, as Fig. 4-4 shows. Their size distribution is limited to values of more than 50 nm. This suggests a small electrochemical surface area (ECSA) due to high particle size.

4.1.4 Rh/C

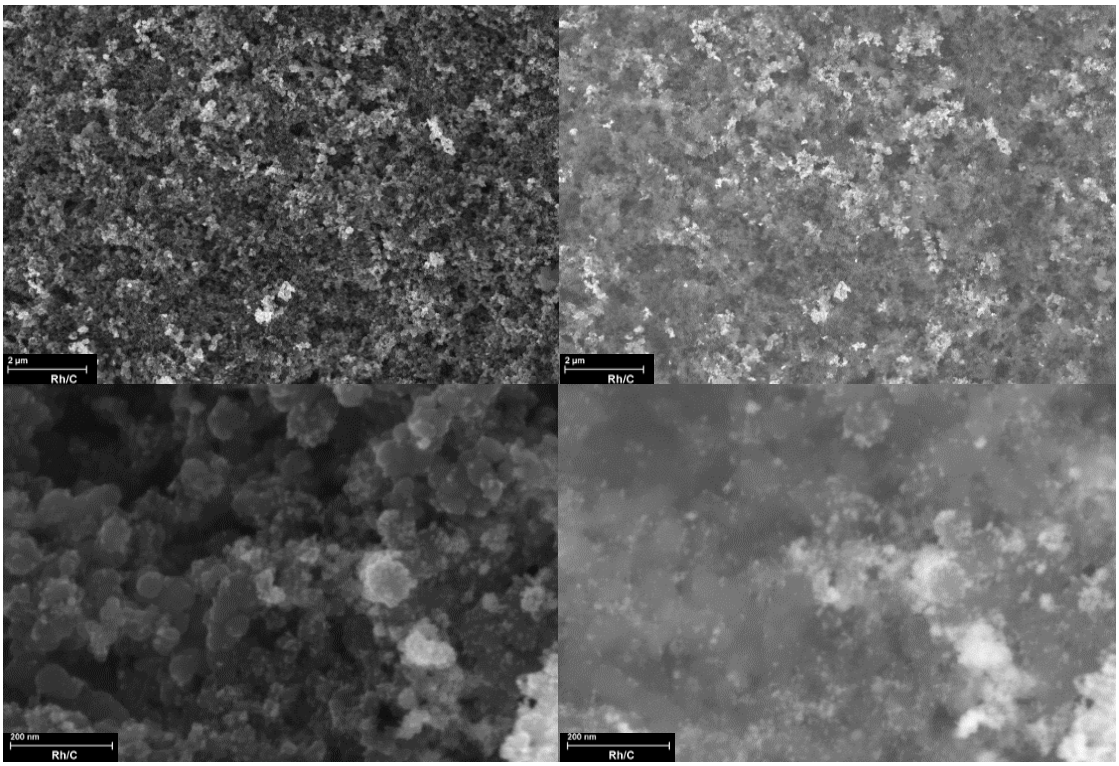

Fig. 4-5: SEM-images of the Rh/C catalyst: left column: in-lens detector images at two magnifications; right column: BSE detector, giving elemental contrast images at two magnifications

As can be seen in the SEM images of Rh/C in Fig. 4-5, the particles have a wide distribution range over the support. Both small particles in the nm range, as well as huge clusters in the micrometre range are present.

4.2 Electrochemical Characterisation of Anode Catalysts

4.2.1 Cyclic Voltammetry

Some of the herein presented Rotating Disk Electrode (RDE) measurements are conducted in collaboration with my partners Maximilian Grandi and Christoph Grimmer. I want to express my gratitude for the assistance and cooperation.

4.2.1.1 Pt/C

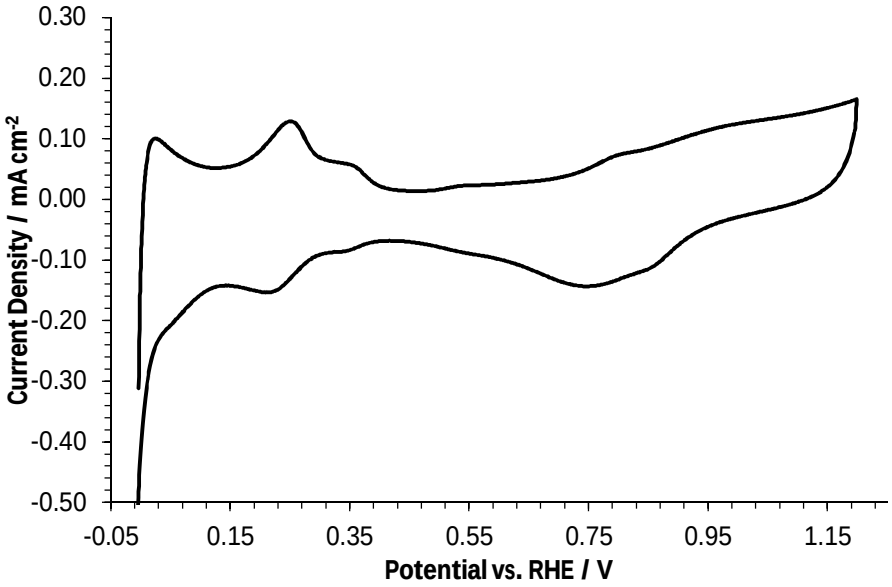

Fig. 4-6: Cyclic voltammogram of Pt/C in deaerated 1 M NaOH at a scan rate of 10 mV s^{-1}

The potential region in the cyclic voltammogram of Pt/C from zero to approx. 0.4 V vs RHE depicts the hydrogen desorption, which is often used as indication for the electrochemical active surface area (ECSA) of platinum surfaces. From 0.4 V vs RHE to about 0.7 V vs RHE no currents occur. Above 0.7 V vs RHE PtOH and PtO are formed. The corresponding reduction of platinum oxide in the region of 0.8 V vs RHE is the first reaction in the cathodic sweep, followed by hydrogen adsorption at approx. 0.15 V vs RHE.

Chatenet et al. [45] and Lima et al. [46] combined several data derived from electrochemical measurements, in-situ Fourier transform infrared spectrometry (in-situ FTIR) and differential electrochemical mass spectrometry (DEMS) to investigate the oxidation of borohydride on bulk gold and platinum electrodes. Their results are in contrast to the widespread belief in literature that the hydrolysis reaction does not occur on Au electrodes [23].

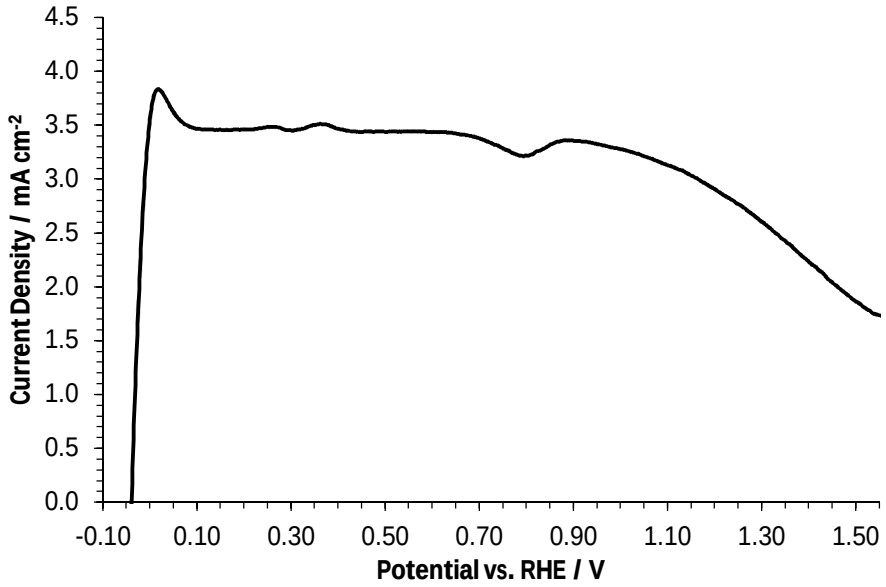

Fig. 4-7: Electrooxidation of borohydride on Pt/C (Anodic Sweep) in 1 M NaOH and 5 mM $NaBH_4$

The electrooxidation of borohydride on Pt/C at hydrostatic conditions is shown in Fig. 4-7. Lima et al. proposed three potential areas of interest during the borohydride oxidation reaction. At the region near OCP, the potential range between 200 and 600-700 mV vs RHE, and the region above 800 mV [46].

In the OCP near region they detected an enormous amount of hydrogen in DEMS, formed due to the partly heterogeneous hydrolysis reaction:

$$BH_4^- + 2H_2O \rightarrow BH_3OH^- + H_2 \quad (11)$$

Between 600 and 700 mV vs RHE they observed both BH_3 and BH_2 spectroscopically at the electrode surface. This fits to the production of BH_3OH^- as product of both possible pathways, the hydrolysis (equation 8) and the first step of regular borohydride oxidation.

$$BH_4^- + OH^- \rightarrow BH_{3,ads} + H_2O + 2e^- \quad (12)$$

$$BH_{3,ads} + OH^- \rightarrow BH_3OH^- \quad (13)$$

BH_3OH^- is oxidised quickly above potentials of 600 mV vs RHE, meaning that hydrogen can only be measured at low anode potentials near OCP.

The fast reaction kinetics on Pt leads to rapid oxidation of H_2 and BH_3OH^-, so the hydrolysis products do not block the Pt surface and BOR is occurring at all potentials.

This is consistent with the results of the electrochemical detection of H_2 on Pt/C investigated during the course of this thesis. (see chapter 4.3) At potentials higher than 800 mV vs RHE, PtOH is present and BOR reaction slows down and low amounts of H_2 are formed.

4.2.1.2 Pd/C

Fig. 4-8 illustrates an exemplary cyclic voltammogram of Pd/C measured in inert 1 M KOH. The downwards peak in the cathodic sweep in the region of 0.7 V vs RHE is characteristic for the reduction of PdO. By integrating this peak area it is possible to determine the electrochemical active surface area (ECSA) of Pd based catalysts.

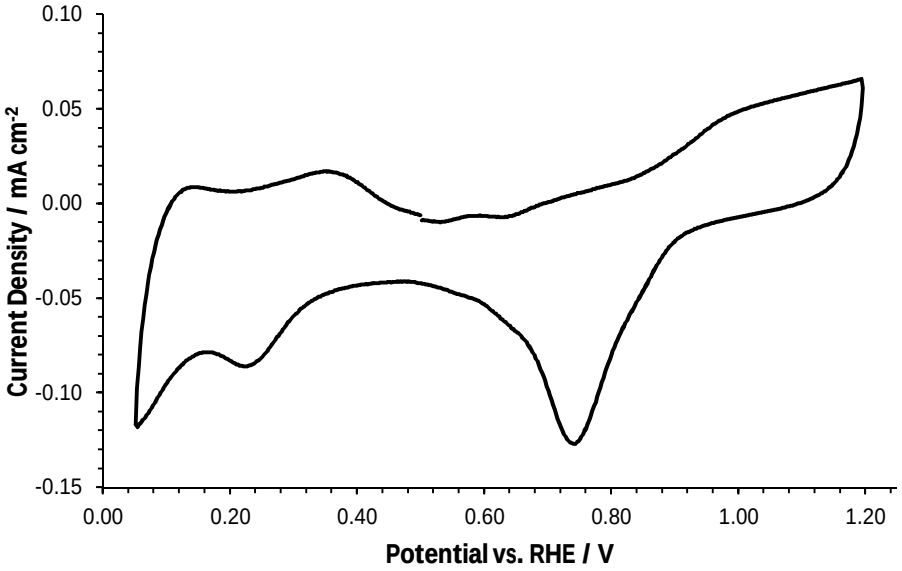

Fig. 4-8: Cyclic voltammogram of Pd/C in deaerated 1 M KOH at a scan rate of 10 mV s^{-1}

Pd/C in 1 M KOH and 5 mM $NaBH_4$ reveals a full eight-electron electrooxidation of the borohydride ion. The persistent borohydride hydrolysis reaction forms intermediates throughout the whole measurement.

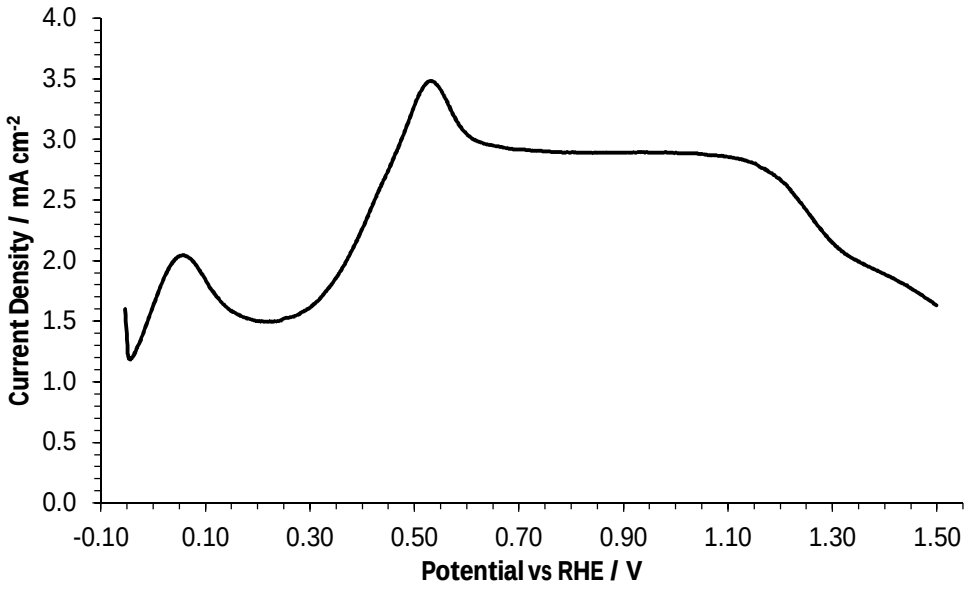

Fig. 4-9: Electrooxidation of borohydride on Pd/C (Anodic Sweep) in 1 M NaOH and 5 mM $NaBH_4$

The current density-potential characteristics of borohydride oxidation on Pd/C are shown in Fig. 4-9. There are three oxidation peaks, which refer to hydrogen oxidation at around 5-10 mV vs RHE, the oxidation of hydrolysis generated BH_3OH^- at 500 mV vs RHE and to the direct eight electron oxidation of borohydride from 0.80 V vs RHE to 1.4 V vs RHE [47].

4.2.1.3 Au/C

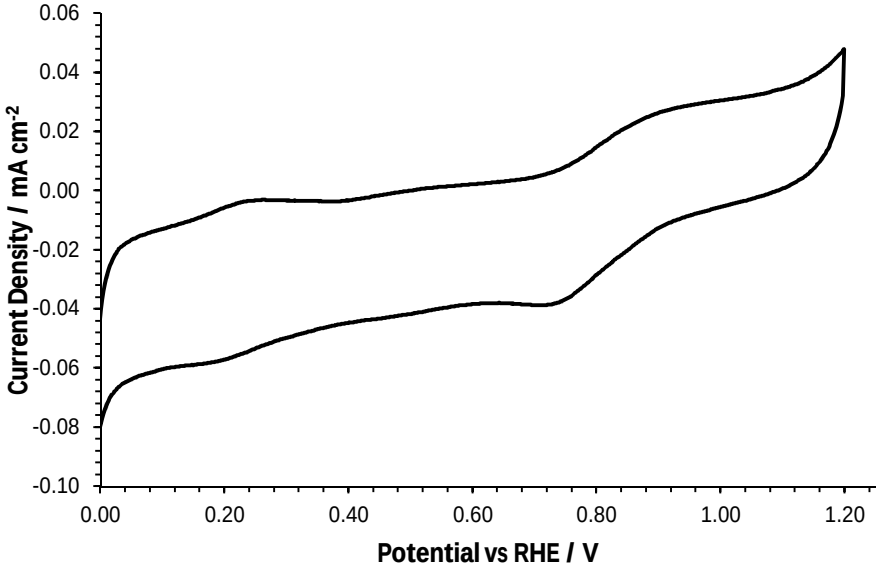

Fig. 4-10: Cyclic voltammogram of Au/C in deaerated 1 M NaOH at a scan rate of 10 mV s^{-1}

Fig. 4-10 shows the cyclic voltammogram of Au/C in 1 M NaOH. In the region of 0.9 V vs RHE the oxidation peak leading to AuO can be seen. The correlated reduction peak at the cathodic sweep is present at around 0.7 V vs RHE.

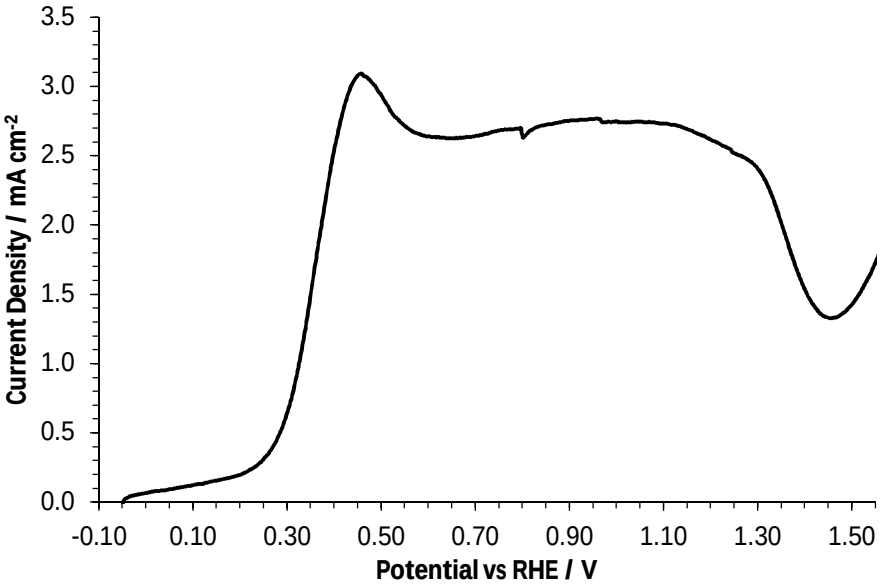

Fig. 4-11: Electrooxidation of borohydride on Au/C (Anodic Sweep) in 1 M NaOH and 5 mM $NaBH_4$

Comparing the borohydride oxidation on Au/C at static conditions (Fig. 4-11) with Pt/C and Pd/C, the absence of the H_2 oxidation peak in the low potential area of 5-10 mV cm^{-2} is observed. According to the conclusions found in literature there is no catalytic activity of Au/C towards the borohydride hydrolysis reaction [23]. Therefore the first oxidation wave (<=0.3 V vs RHE - 0.5 V vs RHE) relates to the full oxidation of borohydride and the second indicates the oxidation of BOR intermediates.

However, Chatenet et al. monitored an unneglectable hydrolysis activity of sputtered gold electrodes during borohydride oxidation. They measured the ex-situ evolution of hydrogen during BOR by coupling online mass spectrometry [45]. This result was confirmed by the real-time hydrogen quantification measurements within this thesis. (see chapter 4.4.1).

Lima et al. proposed the oxidation wave between 0.3 and 0.5 V vs RHE to be related to heterogeneous partly hydrolysis of BH_4^-, generating H_2 and BH_3OH^- followed by their oxidation. The second oxidation wave, spreading from its onset of around 0.5 V vs RHE is assumed to be the real onset potential of direct electrochemical BOR [46].

4.2.1.4 Ru/C

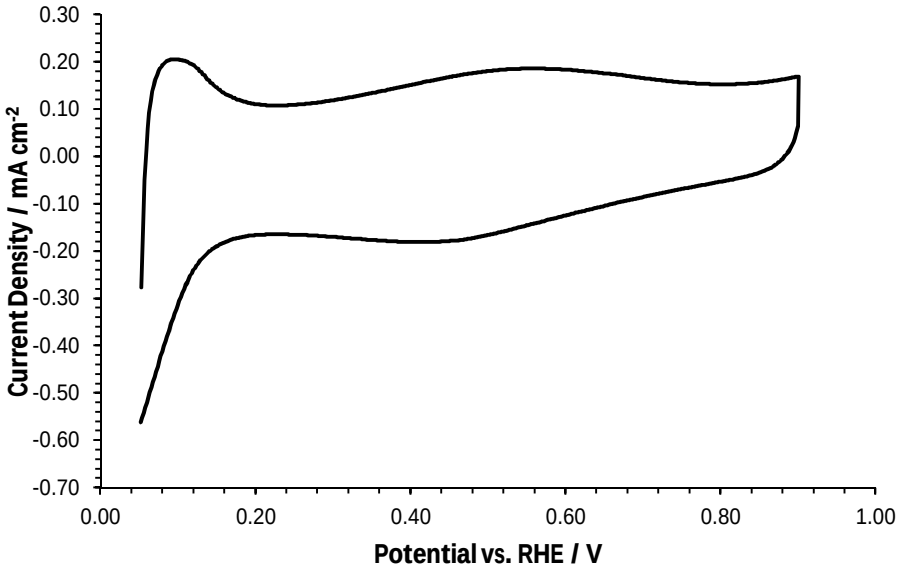

Fig. 4-12. Cyclic voltammogram of Ru/C in deaerated 1 M NaOH at a scan rate of 10 mV s^{-1}

The cyclic voltammogram of Ru/C in alkaline medium does not show assignable information. The oxidation peak at around 0.10 V vs RHE refers to the irreversible oxidation of impurities (no corresponding reduction peak) or the hydrogen oxidation reaction.

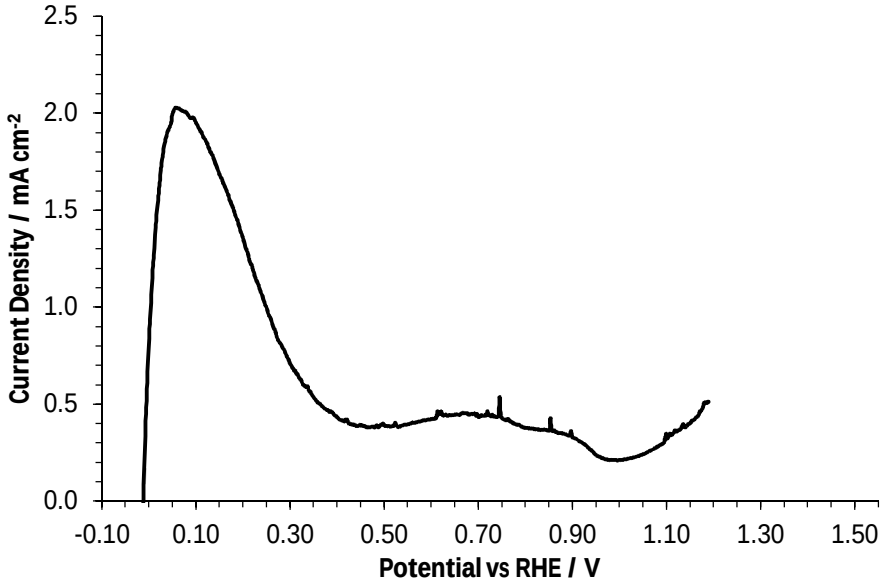

Fig. 4-13: Electrooxidation of borohydride on Ru/C (Anodic Sweep) in 1 M NaOH and 5 mM $NaBH_4$

The hydrostatic borohydride oxidation characteristics on Ru/C in Fig. 4-13 shows an oxidation peak at low potentials from -0.05 V vs RHE to approx. 0.3 V vs RHE. Further Levich and Koutecky-Levich analysis in the next chapter show that this peak refers to the direct (eight-

electron) oxidation of borohydride. No further electrochemical activity can be observed above the potential of 300 mV vs RHE. Literature suggests that the formation of $Ru(OH)_3$ on the catalyst surface causes the inactivity for BOR at potentials greater than 0.3 V vs RHE [44,48].

4.2.1.5 Rh/C

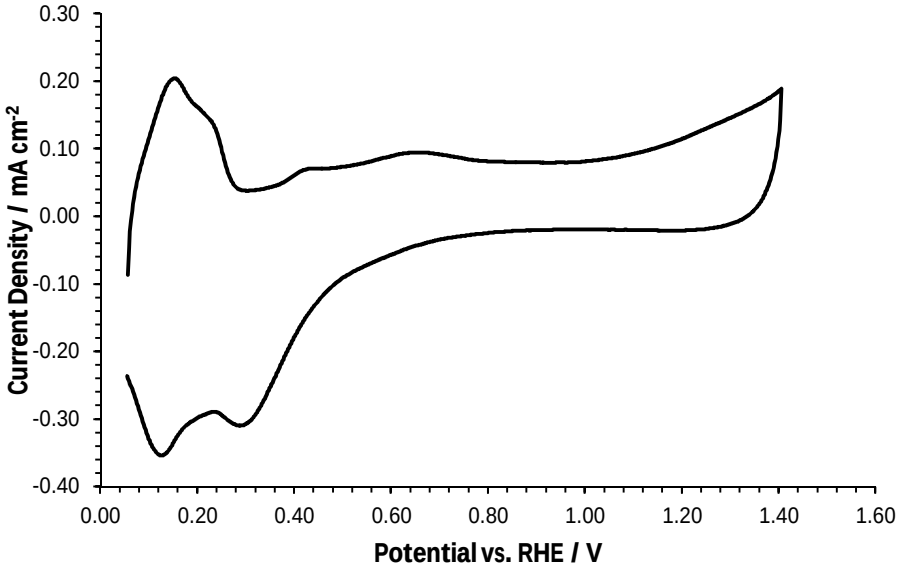

Fig. 4-14: Cyclic voltammogram of Rh/C in deaerated 1 M NaOH at a scan rate of 10 mV s^{-1}

Cyclic voltammogram of Rh/C (Fig. 4-14) shows similarities to the CV of Pt/C (Fig. 4-6). At low potentials in the anodic sweep from zero to about 0.3 V vs RHE hydrogen desorption occurs and the broad peak from 0.3 V vs RHE to about 0.7 V vs RHE is related to surface oxidation. At the cathodic sweep, the currents of oxide reduction and hydrogen adsorption from 0.4 V vs RHE to 0 V vs RHE overlap [49].

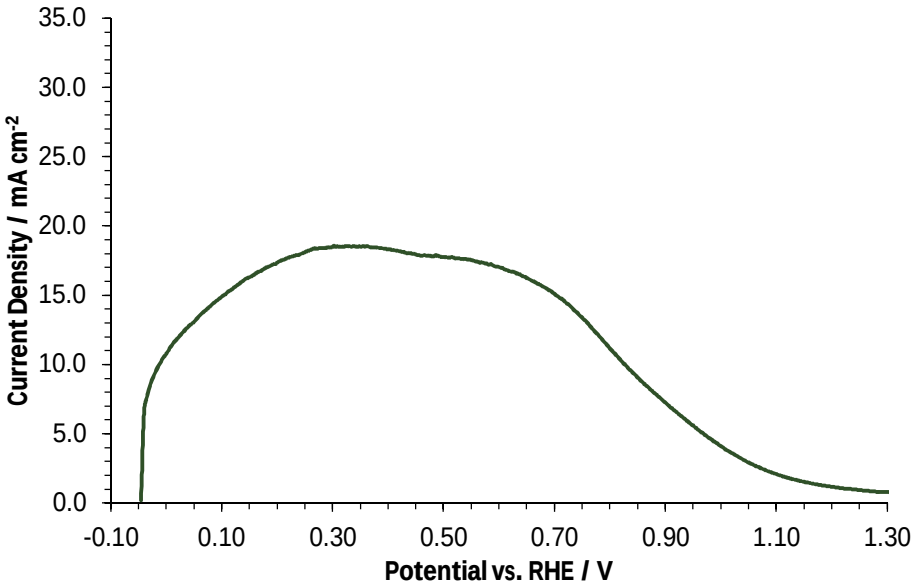

Fig. 4-15: Electrooxidation of borohydride on Rh/C (anodic sweeps) at 400 rpm in 1M NaOH and 5mM $NaBH_4$

Borohydride Oxidation on Rh/C electrodes occurs in a seven electron oxidation wave from the negative potential to 1.1 V vs RHE, with a maximum at about 0.3 V vs RHE. To the author's knowledge there are no publications concerning the BOR mechanism on Rh in literature.

4.2.2 RDE experiments

	Potential vs. RHE [V]	n (Levich)	n (Koutecky-Levich)	k_h [10^{-2} cm s^{-1}]
Pt/C	0.01	-	7.23	0.5
	0.10	6.38	8.55	1.6
	0.20	7.08	7.81	6
	0.40	7.08	7.75	14
	0.55	7.09	7.75	14
	0.73	6.97	7.72	11
	0.83	6.44	7.16	4.16
Ru/C	0.01	8.26	8.26	0.8
	0.18	8.28	8.79	6.1
Pd/C	0.40	4.21	4.73	6.2
	0.55	5.74	7.49	2.2
	0.83	7.82	-	-
Rh/C	0.2	6,15	5.98	6.0
	0.33	6,71	-	-
Au/C	0.73	4.81	7,45	14
	1.05	7.22	7,32	28

Table 4-1: Levich and Koutecky-Levich results for BH_4^- oxidation on investigated catalysts

4.2.2.1 Pt/C

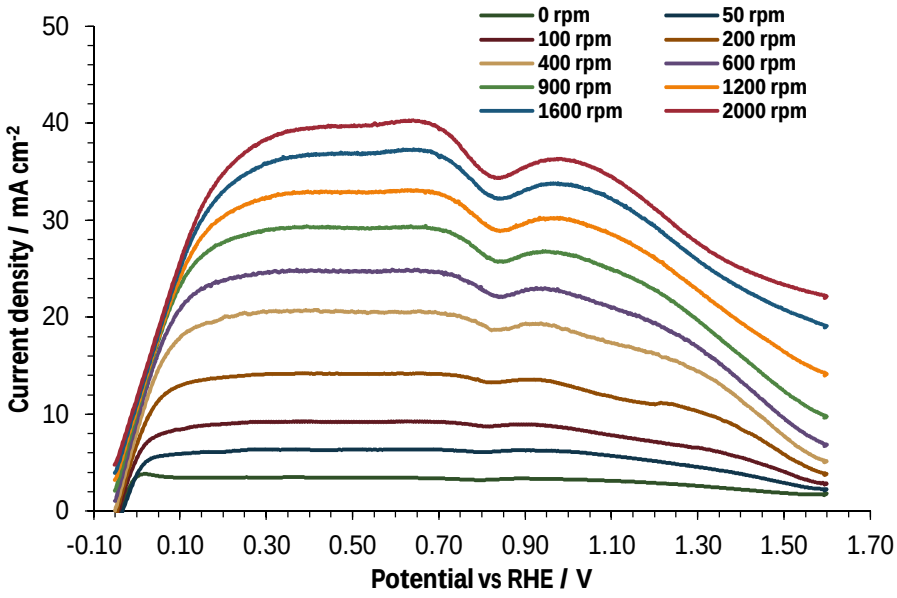

Fig. 4-16: RDE experiments of Pt/C at 0-2000 rpm with a scan rate of 10 mV s^{-1} (5 mM $NaBH_4$)

The RDE measurements were carried out at nine rotation speeds from 0 up to 2000 rpm in 1 M NaOH containing 5 mM $NaBH_4$ (shown in Fig. 4-16). Levich and Koutecky-Levich Plots show an eight electron oxidation on Pt/C in the range up to 0.8 V vs RHE.

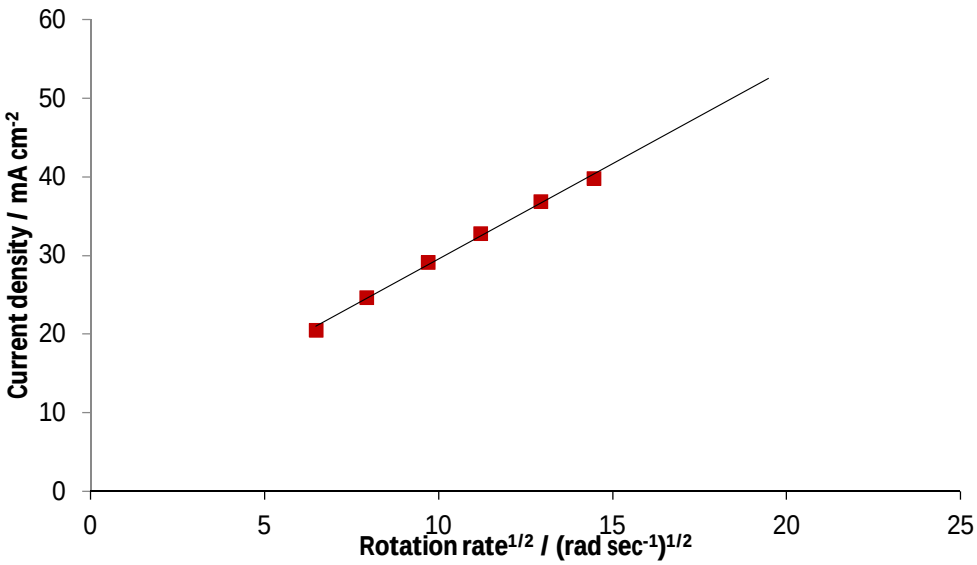

Fig. 4-17: Levich plot of Pt/C at 0.5 V vs RHE

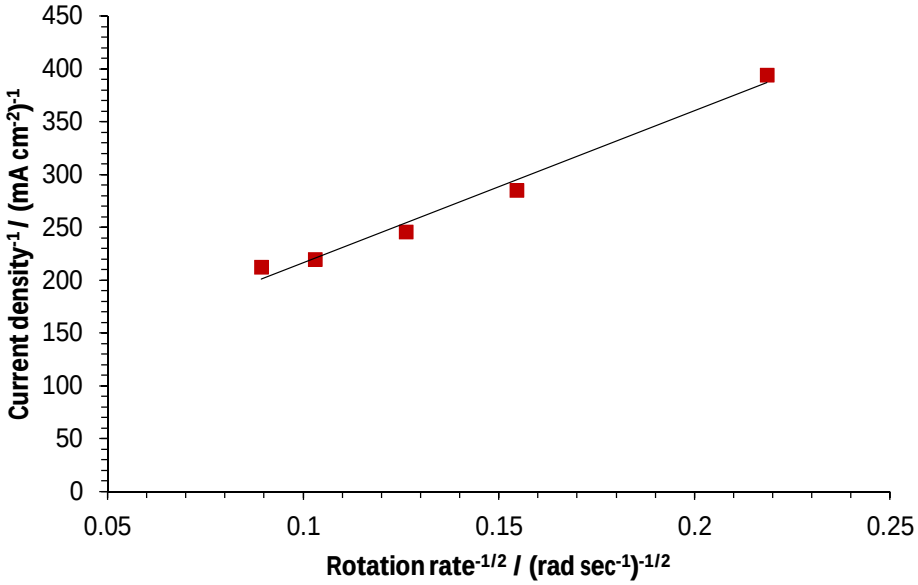

Fig. 4-18: Koutecky-Levich plot of Pt/C at 0.1 V vs RHE

4.2.2.2 Pd/C

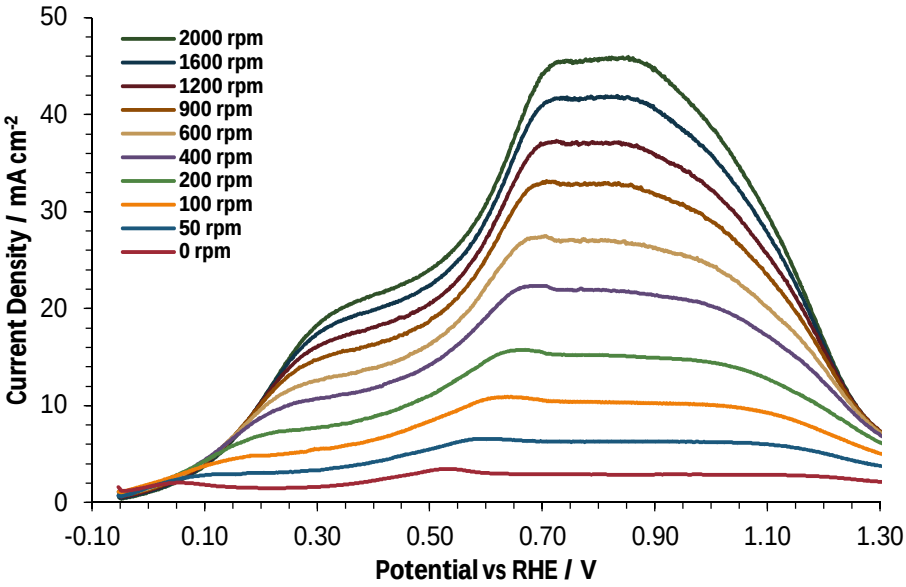

Fig. 4-19: RDE experiments of Pd/C at 0-2000 rpm with a scan rate of 10 mV s^{-1} (5 mM $NaBH_4$)

The RDE measurements were conducted at nine rotation speeds between 0 and 2000 rpm in 1 M NaOH containing 5 mM $NaBH_4$. The anodic sweeps of a characteristic RDE cyclovoltammogram is depicted in Fig. 4-19. Pd/C shows two oxidation waves at around 0.4 V vs RHE and 0.8 V vs RHE and an onset potential of 0.05 V vs RHE, 0.1 V higher than Pt/C. An electrocatalytic window of around 1.4 V can be observed, containing two diffusion limited areas. Levich and Koutecky-Levich plots are shown in Fig. 4-20 and Fig. 4-21 and the resulting parameters are summarised in Table 4-1.

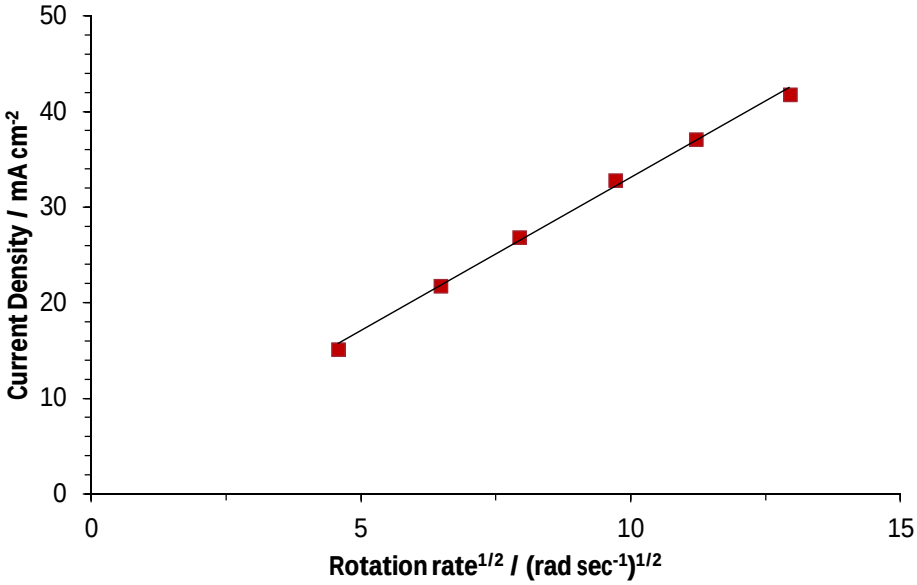

Fig. 4-20: Levich plot of Pd/C at 0.8 V vs RHE

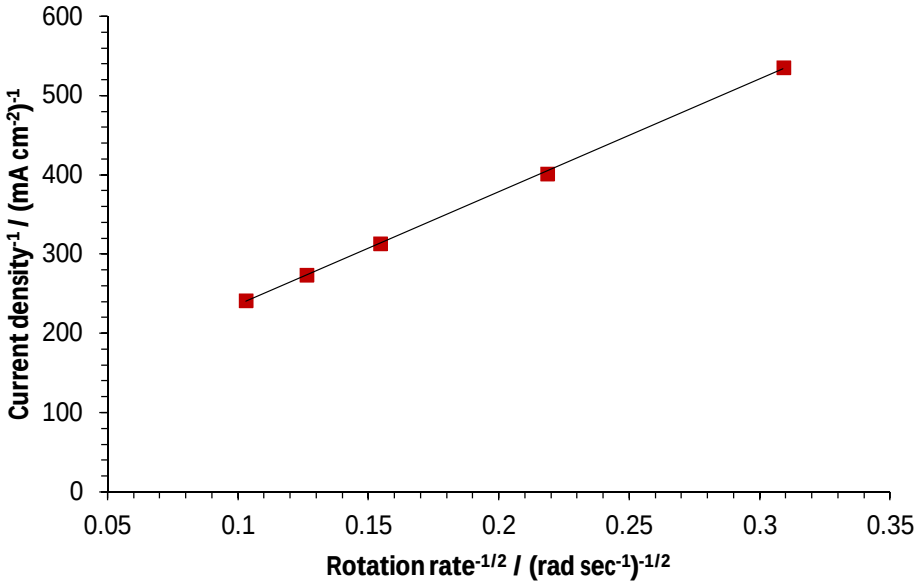

Fig. 4-21: Koutecky-Levich plot of Pd/C at 0.55 V vs RHE

4.2.2.3 Ru/C

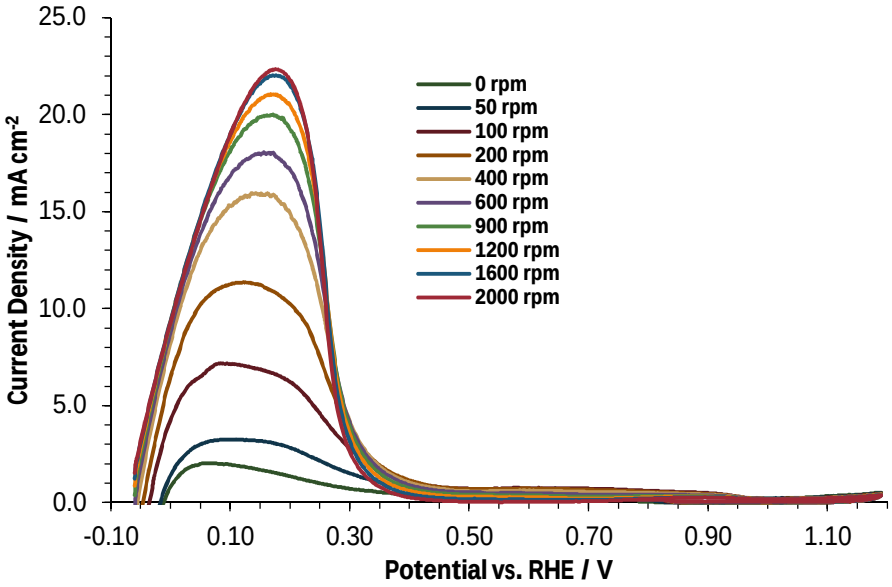

Fig. 4-22: RDE experiments of Ru/C at 0-2000 rpm with a scan rate of 10 mV s^{-1} (5 mM $NaBH_4$)

Ru shows an eight electron oxidation of borohydride in a narrow active potential window from -5 mV vs RHE to about 300 mV vs RHE, as Levich and Koutecky-Levich analysis confirm (Fig. 4-23 and Fig. 4-24).

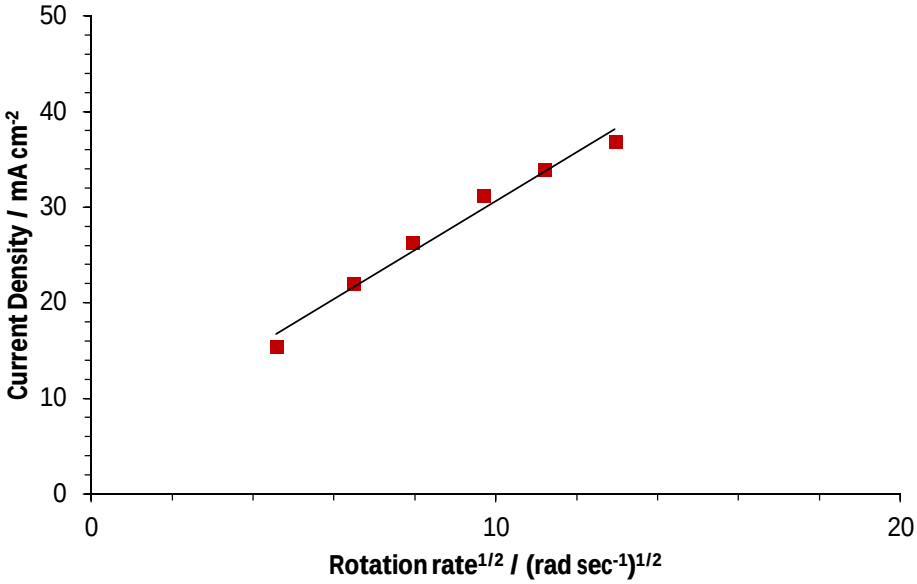

Fig. 4-23: Levich plot of Ru/C at 0.18 V vs RHE

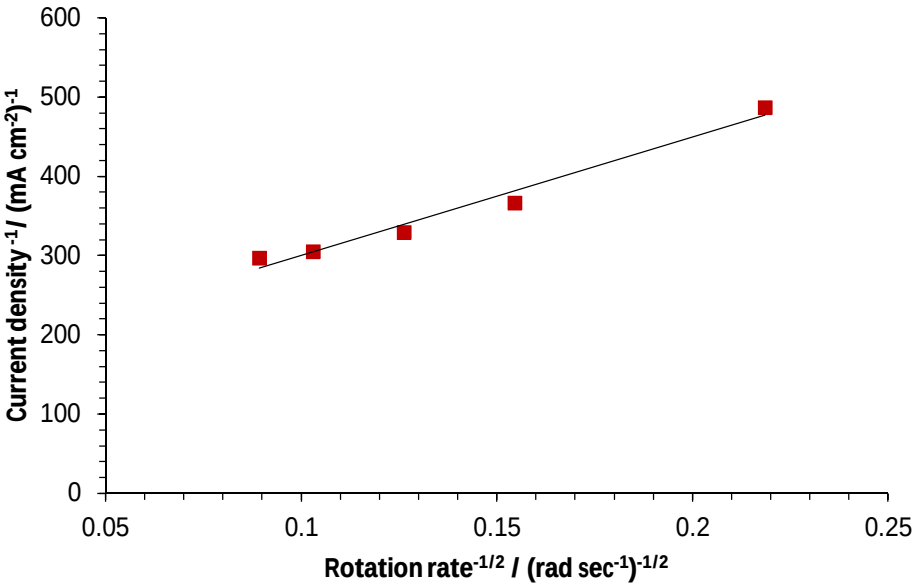

Fig. 4-24: Koutecky-Levich plot of Ru/C at 0.18 V vs RHE

4.2.2.4 Au/C

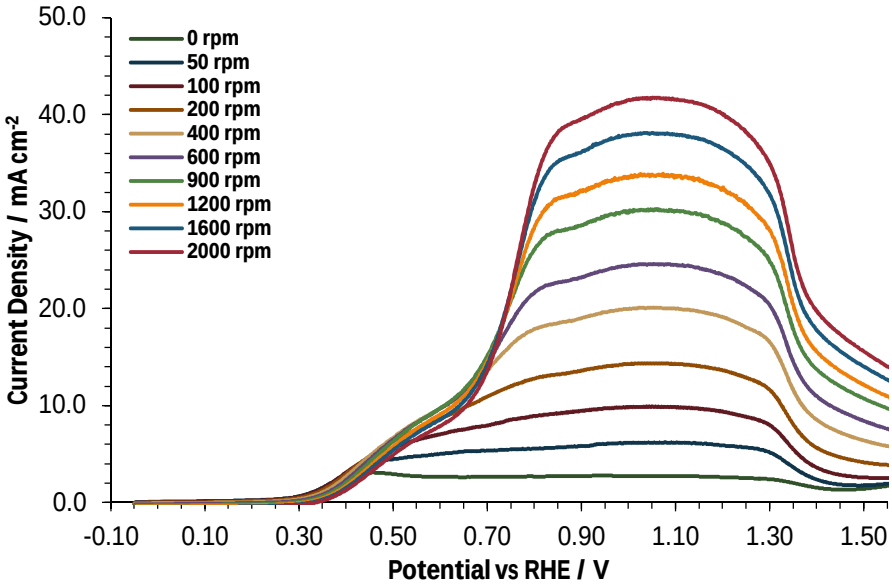

Fig. 4-25: RDE-measurements of Au/C at 0-2000 rpm

Due to the proposed CE-mechanism (partial hydrolysis followed by electrooxidation) of BOR in the potential region of 0.3-0.5 V vs RHE the products of partial hydrolysis are present at the electrode/electrolyte interphase. They are oxidised consecutively requiring a minimum retention time. This time is only given at hydrostatic conditions, in hydrodynamic conditions the additional convection forces the molecules off the electrode. Therefore, a higher potential is needed for the compensation of faster reaction rates and the BOR onset potential increases. Fig. 4-25 illustrates this movement of the onset potential along with rising rpm values according to Lima et al. [45].

Another reason for the shifting onset potential towards higher regions could be the oxidation of impurities on the electrode surface. Due to higher mass transport caused by the additional convection in the solution at higher rotation speeds more impurities are present at the electrode surface, which causes a higher onset potential of the BOR.

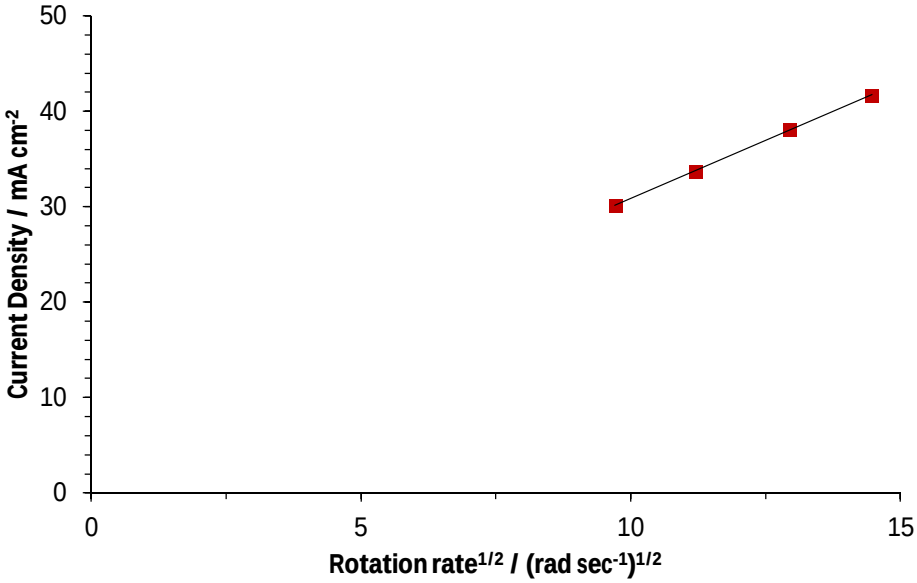

Fig. 4-26: Levich plot of Au/C at 1.05 V vs RHE

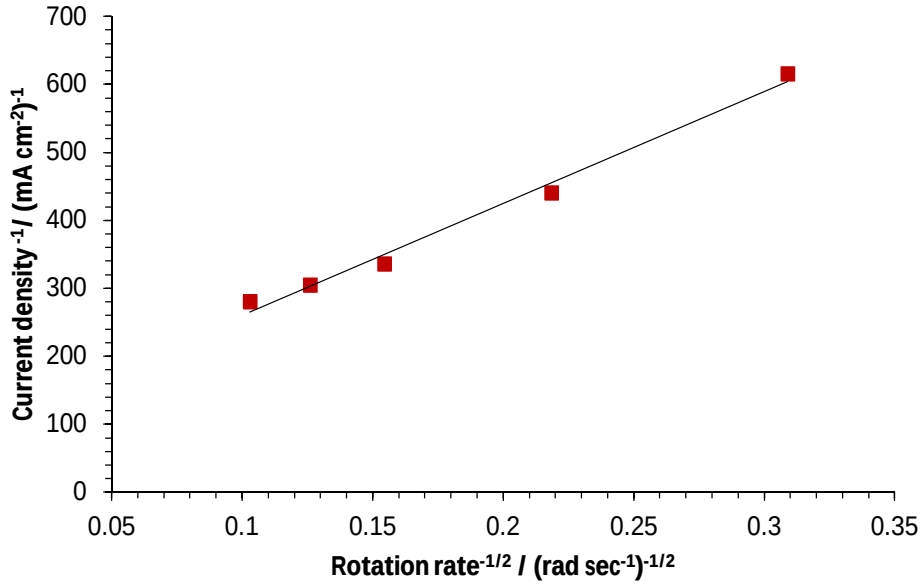

Fig. 4-27: Koutecky-Levich plot of Au/C at 0.73 V vs RHE

4.2.2.5 Rh/C

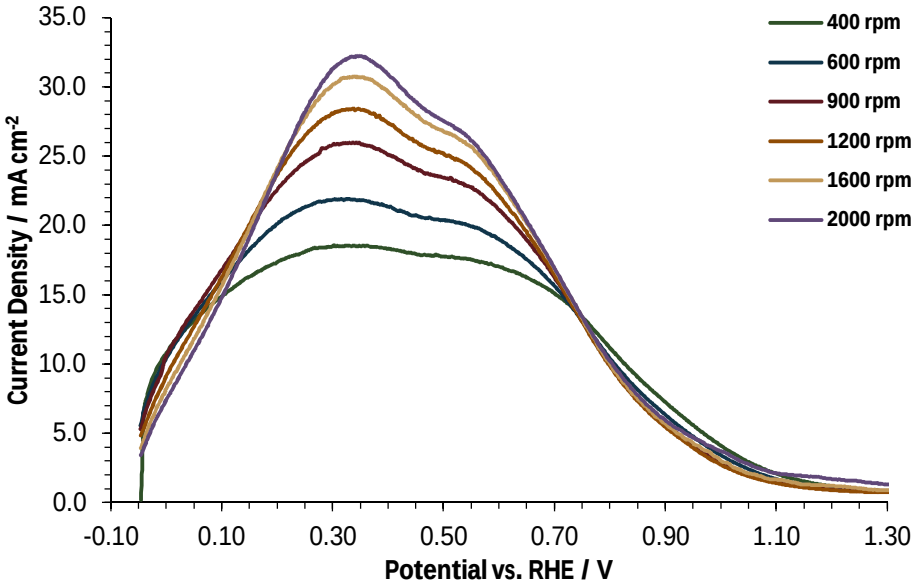

Fig. 4-28: RDE experiments of Rh/C at 0-2000 rpm with a scan rate of 10 mV s^{-1} (5 mM $NaBH_4$)

With higher rotation speeds in the RDE-diagram of Rh/C two oxidation waves can be seen. At a potential of 30 mV vs RHE, the first oxidation wave reaches its maximum in a diffusion limited area, with a six electron oxidation according to Levich analysis. The second oxidation wave forms at potentials of about 0.5 V vs RHE, which is also the onset potential of Rh surface oxidation. Therefore, the lower BOR activity of Rh/C in the higher potential range is most likely associated to the formation of RhOH and RhO.

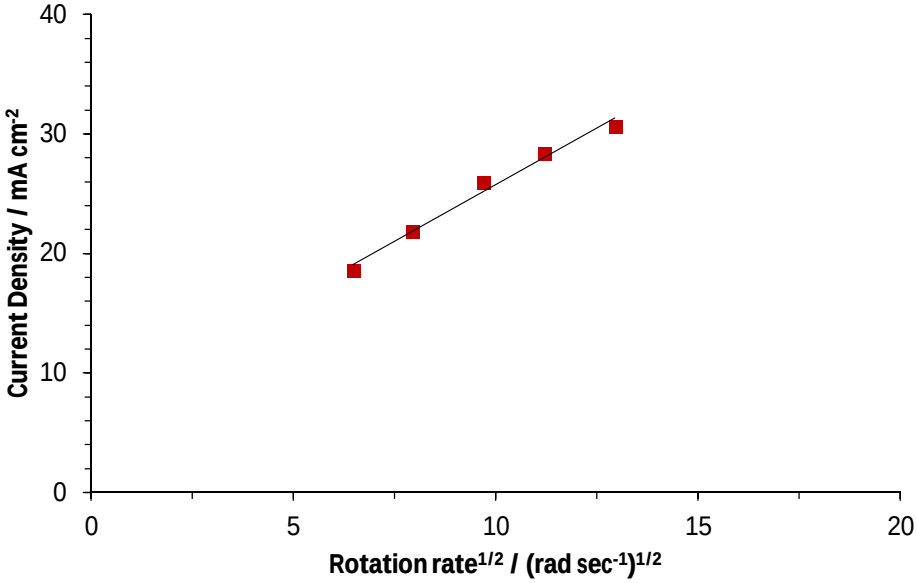

Fig. 4-29: Levich plot of Rh/C at 0.33 V vs RHE

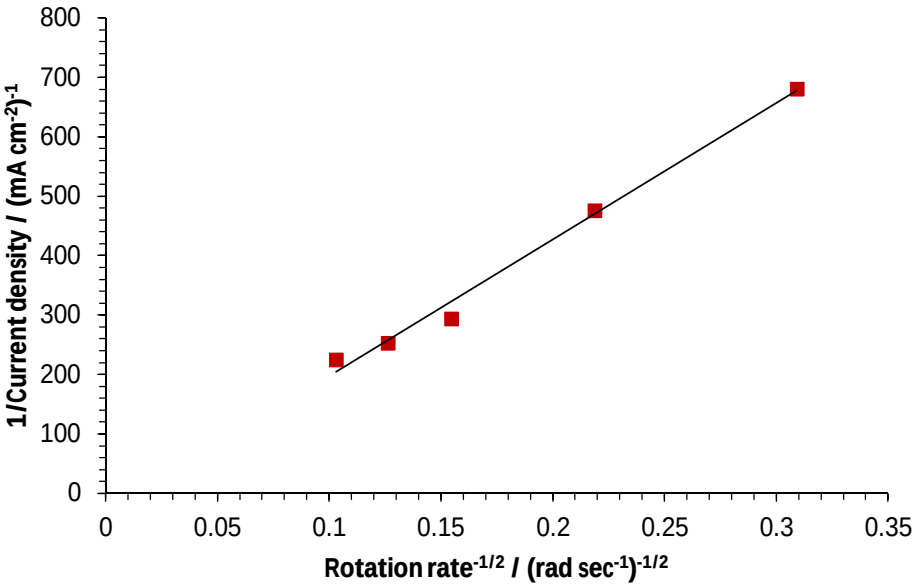

Fig. 4-30: Koutecky-Levich plot of Rh/C at 0.2 V vs RHE

4.3 Electrochemical Characterisation of Cathode Catalysts

MnO_2/C and Ag-Mn_3O_4/C were synthesised and compared with commercial Pt/C and $LaSrMnO_3$/C in terms of ORR activity and borohydride tolerance, employing cyclic voltammetry and RDE-measurements.

The main limitation of these measurements was the necessity of higher metal oxide catalyst loadings on the RDE than experimentally possible to get reasonable results with. According to Mayrhofer et al. [39], too low catalyst loadings result in uncovered regions on the glassy carbon electrode causing a complex behaviour depending on the catalyst distribution and thus the impossibility of mathematical analysis.

To achieve a full surface coverage on the glassy carbon electrode, higher loadings than 112 µg cm^{-2} have to be applied. This would lead to an unstable catalyst layer. Therefore it was not possible to applicate Levich and Koutecky-Levich analysis.

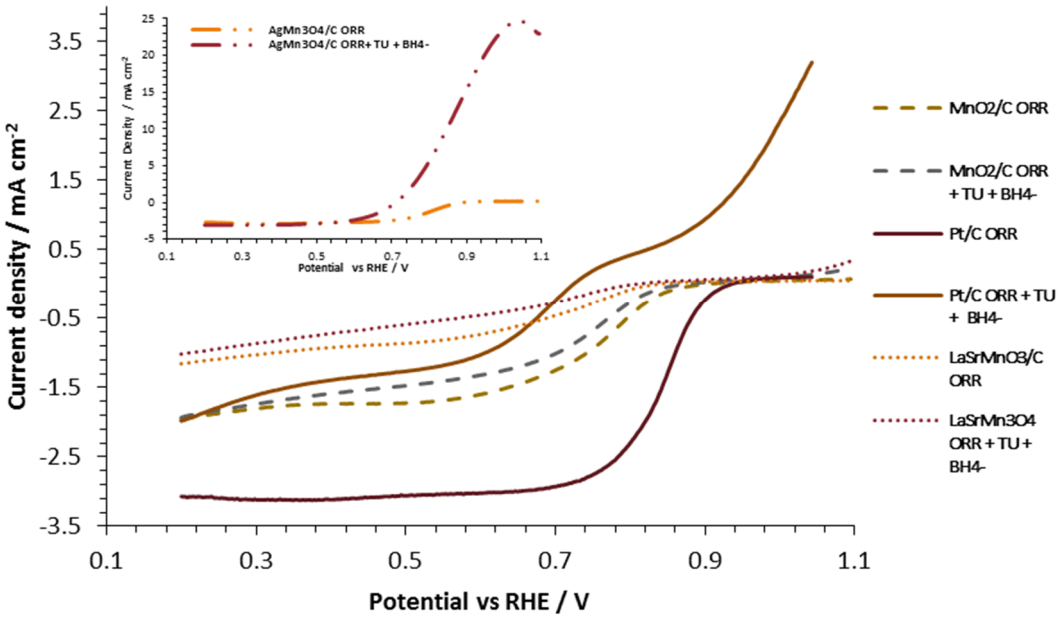

Fig. 4-31: RDE curves at 1600 rpm for ORR on Pt/C, MnO_2/C, $AgMn_3O_4$/C (inlet) and $LaSrMn_3O_4$/C in 1 M NaOH and 1 M NaOH + 5mM $NaBH_4$ + 5 mM TU

Pt/C shows the best performance in ORR catalysis but has no tolerance to borohydride as Fig. 4-31 reveals. $AgMn_3O_4$ exhibits rigorous oxidation currents in potential regions higher than 700 mV vs RHE and a low onset potential.

These results show that Pt/C and $AgMn_3O_4$ are not suitable as cathode catalyst in DBFCs. Low OCVs caused by the ORR onset potential, low power densities and a loss of fuel due to borohydride oxidation are known issues and need to be avoided by the right choice of catalyst.

The ORR on $LaSrMnO_3$ seems indeed tolerant for the presence of borohydride and TU but reveals both a low onset potential and low reduction current densities. MnO_2 showed good ORR activity despite the presence of borohydride and TU in the electrolyte, exhibiting the lowest potential and current losses

Summing up the results, MnO_2 has the best ORR onset potential at about 0.8 V vs RHE and also the highest ORR current density in presence of borohydride and TU, additionally negative effects due to borohydride oxidation are not expected. Therefore MnO_2/C was chosen as the cathode active layer in the DBFC mixed electrolyte measurement cell.

4.4 Fuel Cell Tests

4.4.1 Polarisation Curves

All polarisation curves were conducted with 1 M NaOH, containing 1 M $NaBH_4$ and 5mM thiourea at ambient temperature and 40°C. Small amounts of TU reduce the borohydride hydrolysis reaction. The generated hydrogen was quantified during recording of the polarisation curves in an external electrochemical hydrogen detection cell.

Fig. 4-32 and Fig. 4-33 show all polarisation curves and all power density curves of the in-situ measurements, respectively. Among the five noble metals Platinum is still the anode catalyst to outperform in direct borohydride fuel cells. The maximum power density of 55 mW cm^{-2} is the highest value during these investigations.

Despite its poor activity in the higher potential range of ex-situ measurements, Ru/C performs well in the single cell tests. Low overpotential losses, a rather high power density of 35 mW cm^{-2} and its low price make ruthenium a potential alternative to Pt/C in DBFCs. The moderate price of Ru enables electrodes with much higher catalyst loadings, which have a comparable power density to Pt/C.

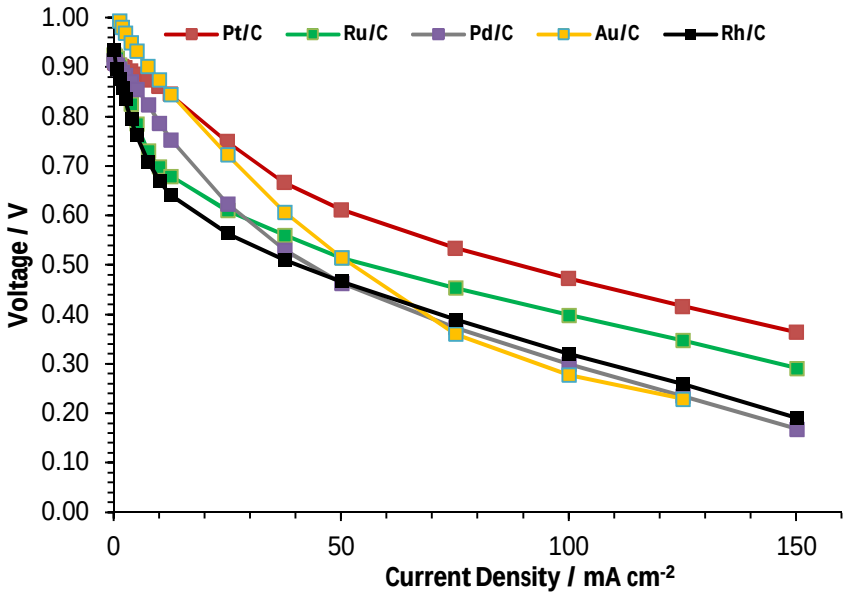

Fig. 4-32: Compared polarisation curves of all fabricated anodes vs MnO_2/C with 1M $NaBH_4$, 1M NaOH and 5mM Thiourea at 40 °C

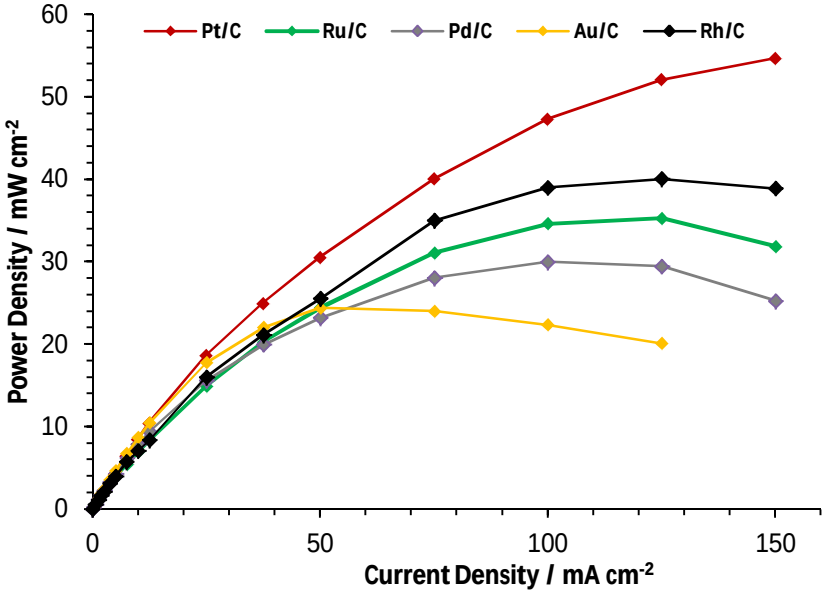

Fig. 4-33: Compared power density curves of all fabricated anodes vs MnO_2/C in 1M $NaBH_4$, 1M NaOH and 5mM thiourea at 40 °C

Additionally, the five anode electrocatalysts were investigated in terms of their activity for the borohydride hydrolysis reaction [23,26], which is competing with the desired BH_4^- oxidation reaction (details see chapter 2.6).

The hydrogen evolution was measured during the record of the polarisation curves (chapter 4.4.1), as a function of the cell voltage. The produced hydrogen was detected by connecting the outlet of the DBFC to the detection cell. This method exhibits a high sensitivity and is not expected to affect the single cell operation.

During all fuel cell measurements the anode potential was recorded via a Luggin capillary and a RHE. Due to ongoing hydrolysis during all measurements and therefore the presence of hydrogen bubbles in the Luggin capillary, the connection to the reference electrode got lost in the measurements of Pd/C, Pt/C and Au/C polarisation at 40 °C and during the Pt/C polarisation at both temperatures.

4.4.1.1 Pt/C

Although Pt is a hydrolysis active metal it can be faradaic efficient as Lima et al. showed [46]. This observation is confirmed by the measurement results in this thesis. The hydrogen detected during the record of Pt/Cs polarisation curve in Fig. 4-35 shows that H_2 only evolves at cell voltages near OCV. This is also the range where the voltage drops in the polarisation curve. (Fig. 4-34).

The results obtained are in agreement with the proposed mechanism of borohydride oxidation on Pt/C, which is described in chapter 4.2.1.1. Hydrogen was detected only in the region around OCP of the anode. At elevated anode potentials the oxidation of H_2 on BH_3OH^- can occur. Consistent with this assumption, no hydrogen was detected above current densities of 20 mA cm^{-2}. (Fig. 4-35)

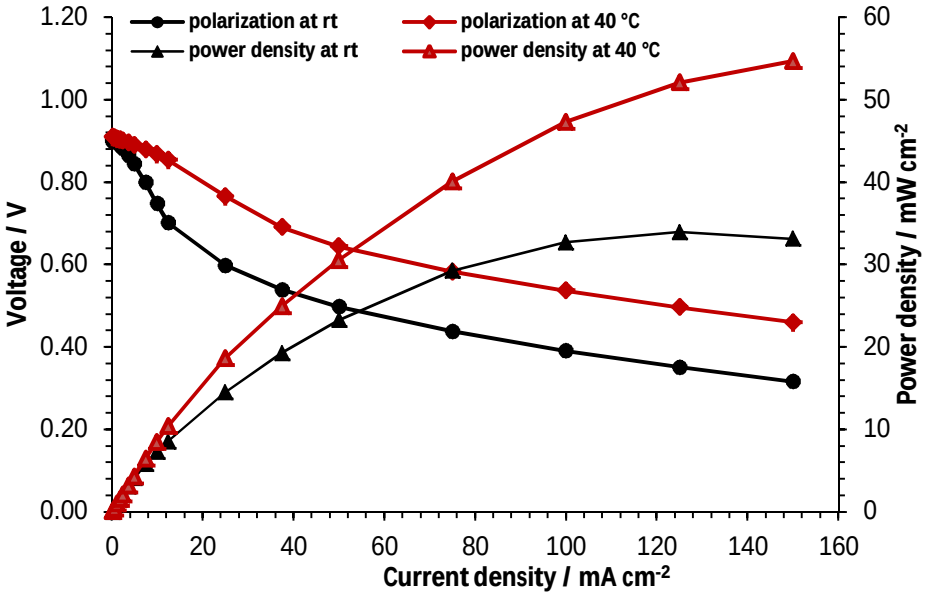

Fig. 4-34: Polarisation curve of Pt/C at ambient temperature and 40 °C

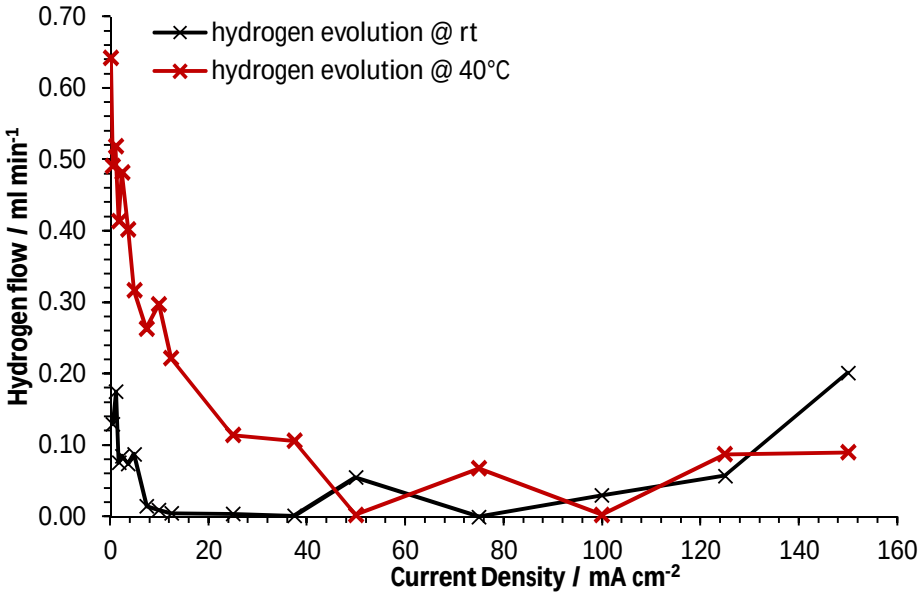

Fig. 4-35: H_2-evolution due to BH_4^- hydrolysis on Pt/C at ambient temperature and 40 °C

As already discussed in section 4.2 the hydrogen evolution on the Pt/C anode was high at low anode potentials and decreased with increasing potential. In the region of the highest current density a slight increase of the hydrogen flow is detected.

4.4.1.2 Ru/C

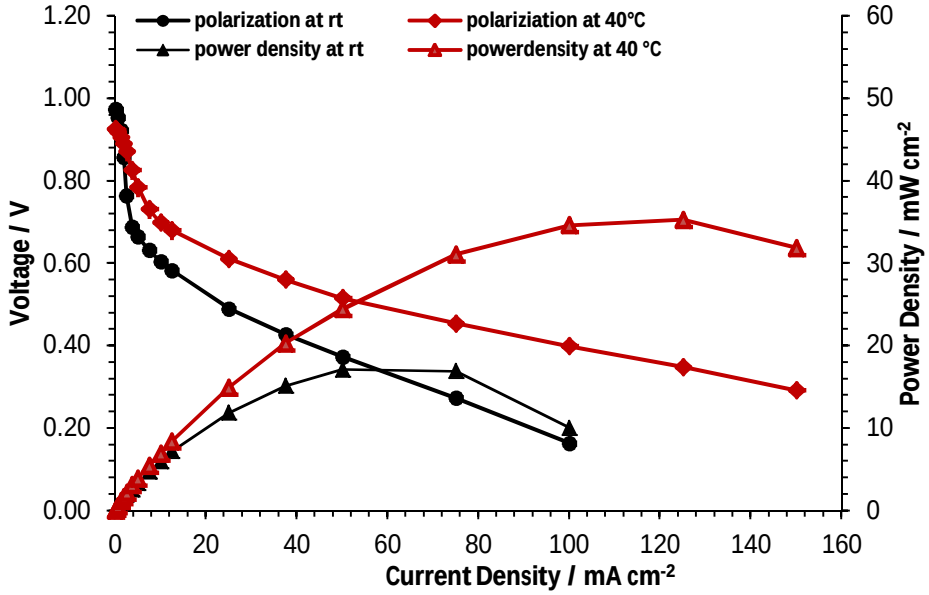

Fig. 4-36: Polarisation curve of Ru/C at ambient temperature and 40 °C

According to Grimmer et al. [44] ruthenium's polarisation curve reveals very low overpotentials in the region of low current densities (Fig. 4-36). Beyond approx. 5 mA cm^{-2}, even earlier at ambient temperature, the voltage drop increases sharply along with the rising anode potential shown in Fig. 4-38. Ex-situ measurements predicted this kind of behaviour. (chapter 4.2.2.3)

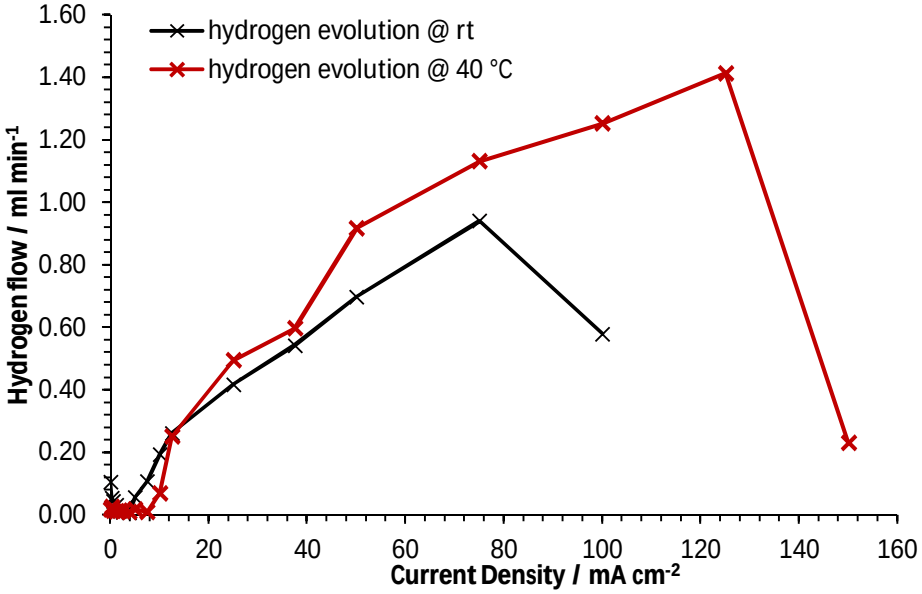

Fig. 4-37: H_2-evolution due to BH_4^- hydrolysis on Ru/C at ambient temperature and 40 °C

As shown in figure Fig. 4-37 the evolution of hydrogen rises vastly above the current density of 5-10 mA cm^{-2}. The increasing inactivity of Ru/C at higher anode potentials also explains why the developed hydrogen is no longer oxidised.

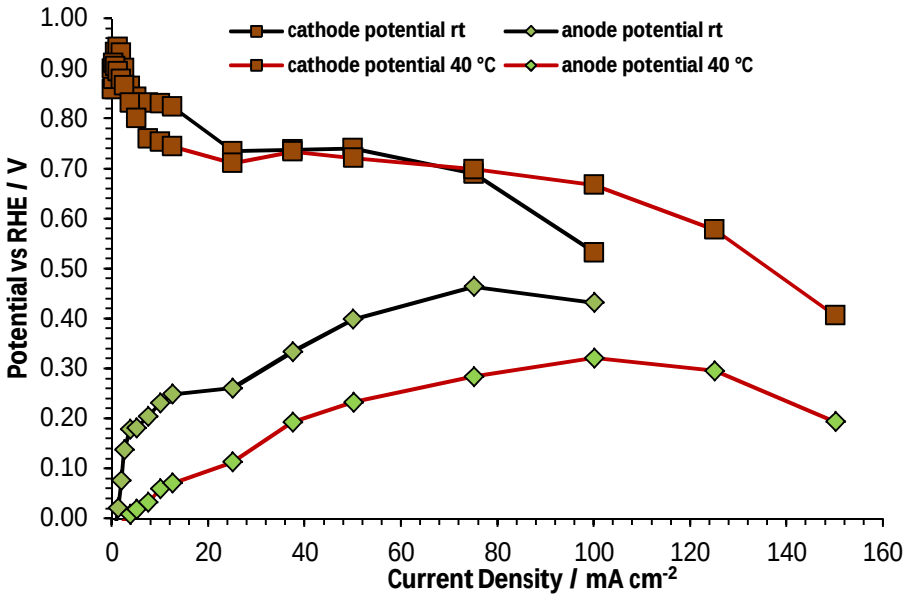

Fig. 4-38: Anode and cathode potential development during polarisation curve of Ru/C vs MnO_2

4.4.1.3 Pd/C

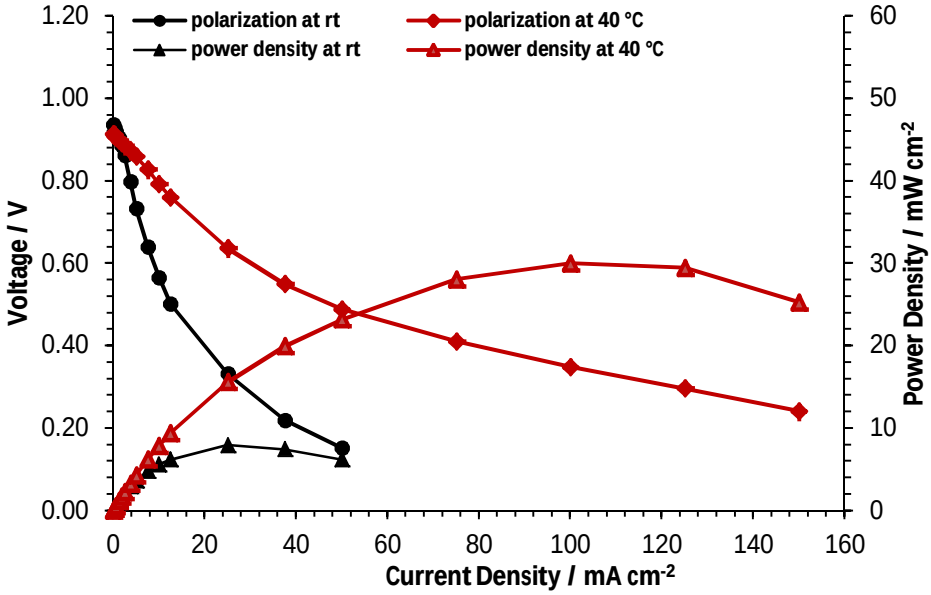

Fig. 4-39: Polarisation Curve of Pd/C at 40 °C

Although Pd/C shows a quite good activity towards borohydride oxidation in ex-situ measurements, the in-situ results were below the expectations. As the development of the anode potential shows in Fig. 4-41 there is an enormous increase at low current densities

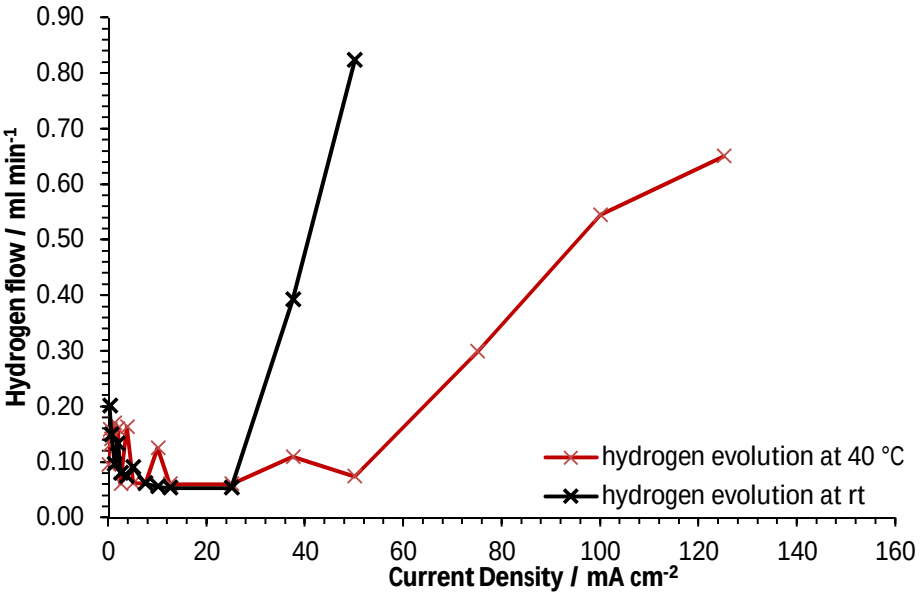

Fig. 4-40: H_2-evolution due to BH_4^- hydrolysis on Pd/C at ambient temperature and 40 °C

By comparing the anode potential (Fig. 4-41: Anode and cathode potential development during polarisation curve of Pd/C vs $MnO_2$with the hydrogen flow at ambient temperature in Fig. 4-40 there is a huge increase of hydrogen development at current densities similar to the increase of

the anode potential. This leads to the conclusion that the bad performance of the Pd/C anode is due to the preference for borohydride hydrolysis over the BOR at room temperature.

At 40 °C the kinetics of BOR accelerates and the hydrolysis reaction seems to be disfavoured compared to lower temperatures. The anode potential was not measurable but a trend to lower potentials is assumed.

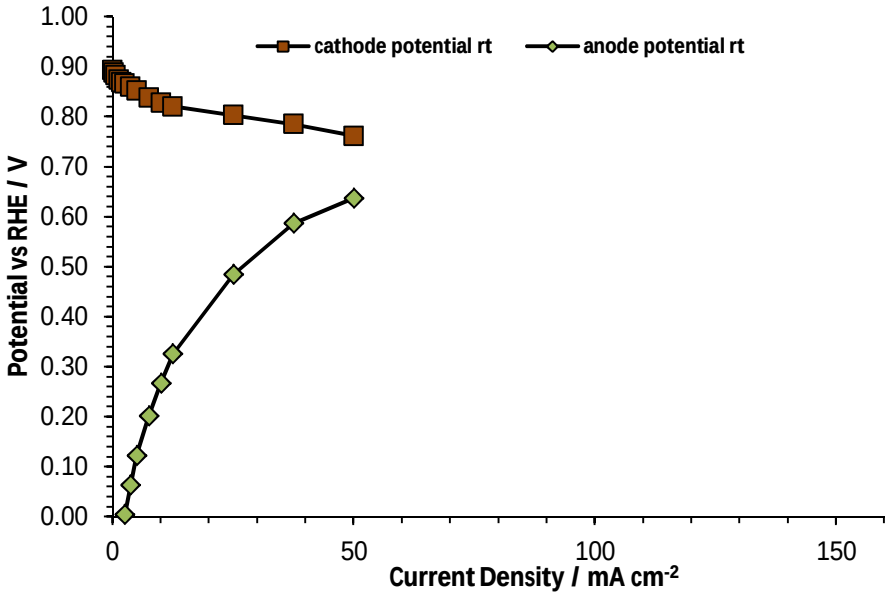

Fig. 4-41: Anode and cathode potential development during polarisation curve of Pd/C vs MnO_2

4.4.1.4 Au/C

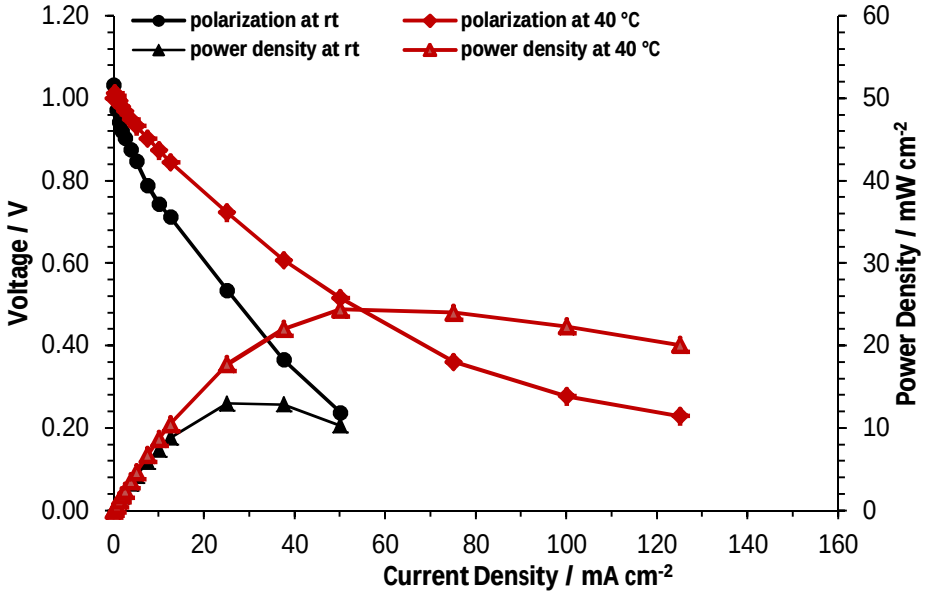

Fig. 4-42: Polarisation Curve of Au/C at room temperature and 40 °C

Whereas borohydride hydrolysis does not seem to harm the efficiency of BOR on Pt, gold behaves contrary in this regard. Chatenet and Lima [45,46] showed in their respective publications the negative impacts during ex-situ measurements namely a blocked anode catalyst layer by hydrolysis generated products due to sluggish kinetics in their oxidation compared to Pt/C was reported.

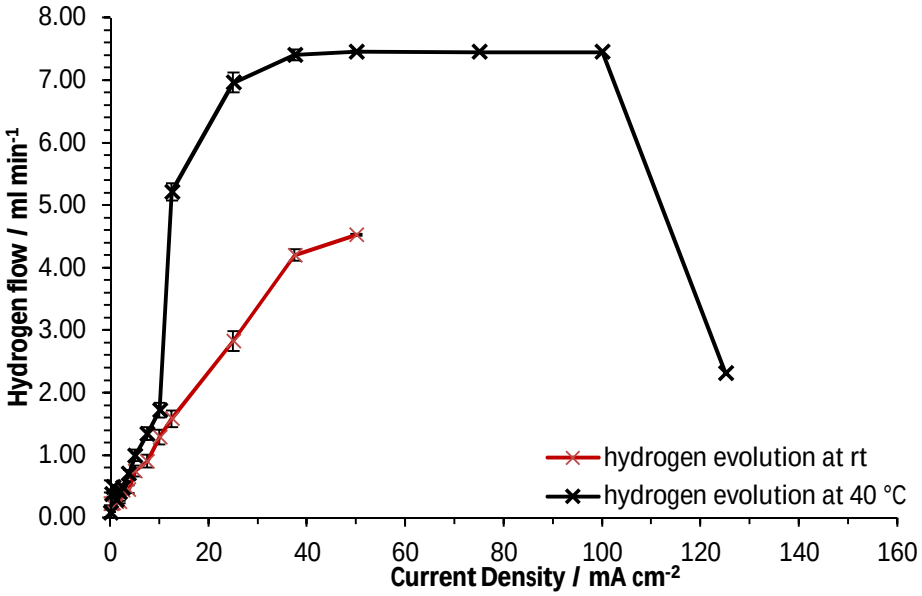

Fig. 4-43: H_2-evolution due to BH_4^- hydrolysis on Au/C at ambient temperature and at 40 °C

These results are confirmed with our in-situ fuel cell measurements, illustrated in Fig. 4-43 where the detection limit for hydrogen is exceeded above current densities of 40 mA cm^{-2}. Gold is the most active catalyst towards hydrolysis among all investigated probes. There is a sharp downwards bending in the polarisation curve and a limit of power density in combination with maximum hydrolysis. (Fig. 4-32 and Fig. 4-33).

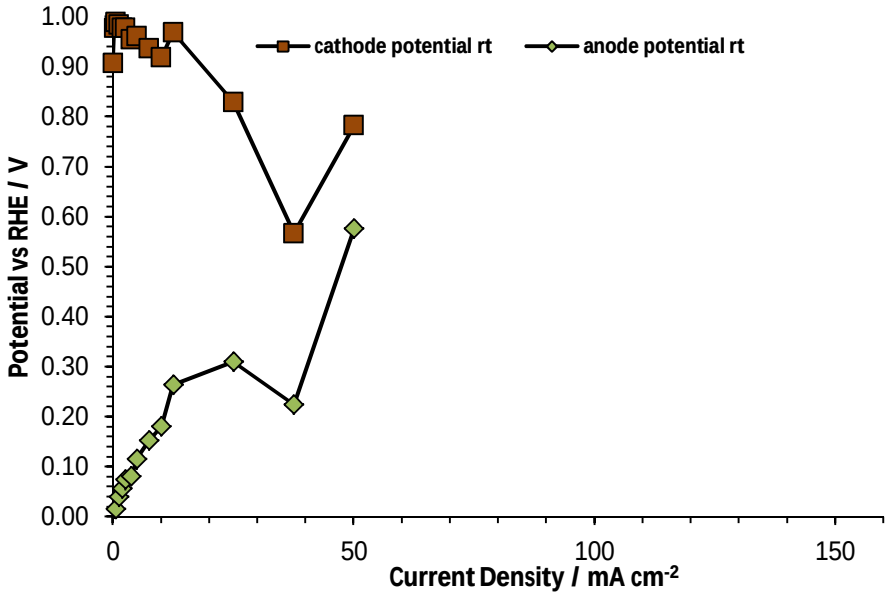

Fig. 4-44: Anode and cathode potential development during polarisation curve of Au/C vs MnO_2

Fig. 4-44 shows the anode and cathode potential during the polarisation of Au/C vs MnO_2. The sharply rising anode potential correlates with the low performance of the polarisation curve. The outliner at 37 mA cm^{-2} is assumed to be a failure during anode potential measurement due to hydrolysis gas bubbles in the Luggin capillary. In contrast to Pt/C, the hydrolysis reaction leads to a blocking of the Au/C surface with the negatively charged BH_3OH^-, resulting in an electrostatic repulsion between the negatively charged surface and the borohydride anion [46].

This can also be linked to the poor polarisation curves in Fig. 4-42 and Fig. 4-44: The maximum current density is 12.9 mW cm^{-2} at ambient temperature and 24.4 mW cm^{-2} at 40 °C resulting in relative power densities of 38 % at ambient temperature and 44 % at 40 °C, compared to Pt/C. (see Fig. 4-35)

4.4.1.5 Rh/C

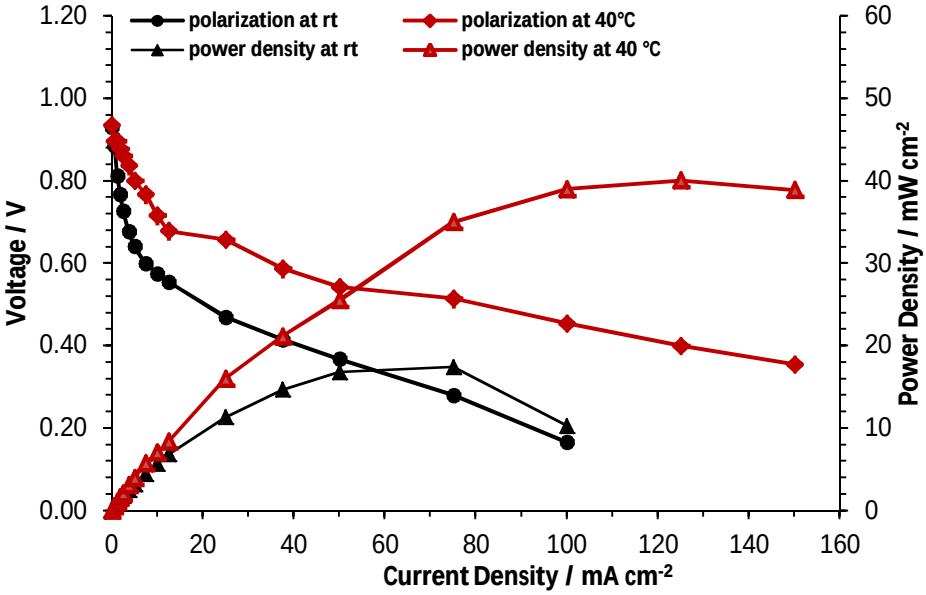

Fig. 4-45: Polarisation Curve of Rh/C at ambient temperature

Rh/C has a high maximum power density of about 40 mW cm^{-2} at 40 °C, which is the double of room temperature maximum power density. Surprisingly the hydrogen development at both temperatures is nearly the same. (Fig. 4-46) This difference is most likely attributed to the large positive effect of temperature on the BOR in contrast to the effect on the hydrolysis reaction. Another explanation is a behaviour comparable to Pt/C anodes, assuming the evolution of hydrolysis products that are oxidised with a high reaction rate. This mechanism has to be clarified by measurements of reaction products at different potentials by FTIR and DEMS.

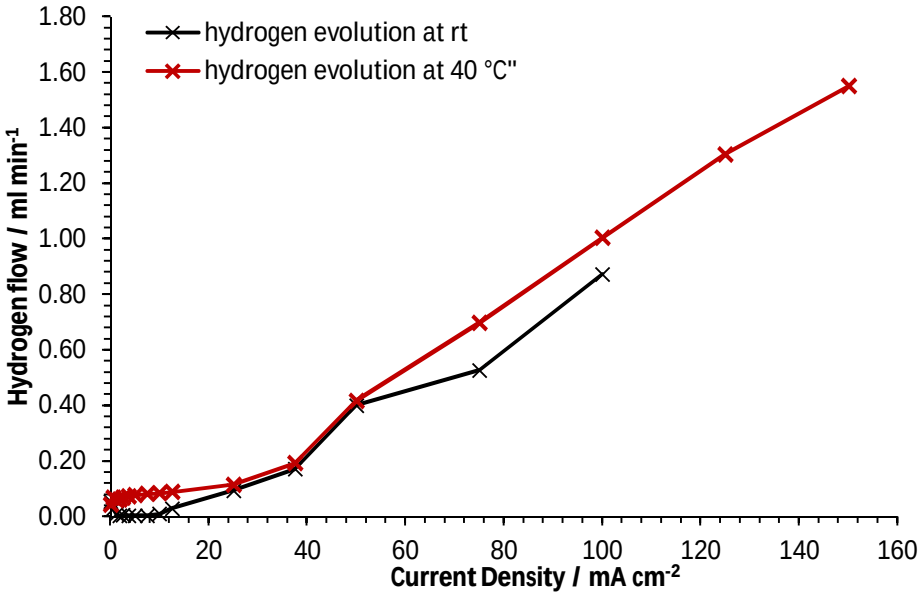

Fig. 4-46: H_2-evolution due to BH_4^- hydrolysis on Rh/C at ambient temperature and 40 °C

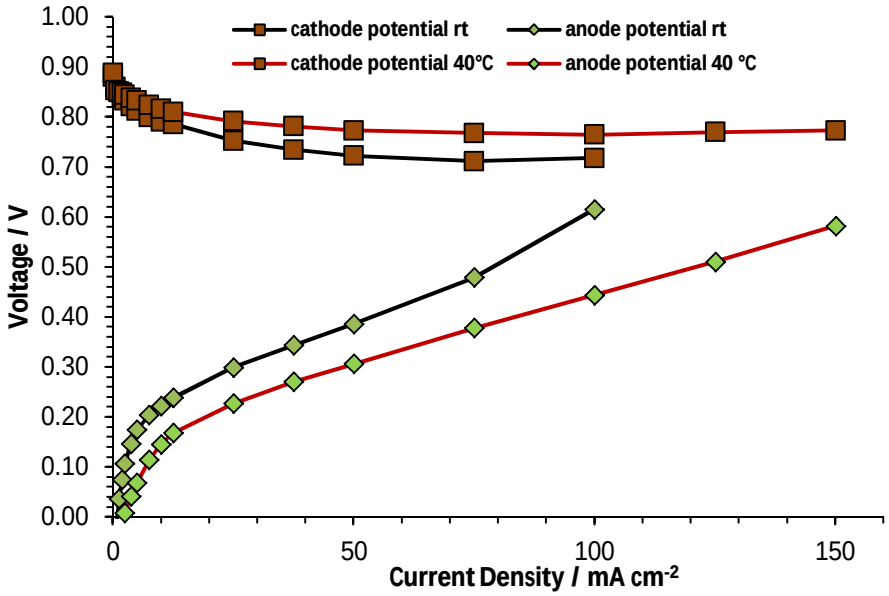

Fig. 4-47: Anode and cathode potential development during polarisation curve of Rh/C vs MnO_2

5 Conclusion

The DBFC utilises the chemical energy in borohydride efficiently by transforming it directly into electricity. Using the liquid borohydride solution as fuel has the advantages of an easy handling, long term stability and high energy density [24]. The main challenge associated with DBFCs is the borohydride hydrolysis side reaction. In this thesis, the in-situ monitoring of hydrolysis activity was performed by the sensitive online measurement of hydrogen evolution [43].

Noble metal anode catalysts for the DBFC were synthesised and characterised ex-situ by cyclic voltammetry and RDE voltammograms and in-situ by polarisation curves in a DBFC in a mixed electrolyte design. The highest power density was achieved with a Pt/C anode catalyst. Ru/C catalysts showed a good performance in in-situ measurements and represent a good alternative to Pt/C electrodes due to the lower price, even when higher catalyst loadings are required.

In addition, some metal-oxide cathode catalysts on carbon support for operation in the DBFC mixed electrolyte were investigated in regards of their borohydride tolerance and their activity towards the oxygen reduction reaction by ex-situ RDE experiments.

During the polarisation of the different anode catalysts in the DBFC, the evolved hydrogen was detected quantitatively. The achieved results revealed a lower hydrogen evolution on Pt/C than expected above current densities of 25 mA cm^{-2}.

Unexpectedly, a very high hydrogen evolution on the Au/C anode that even exceeded the detection limit of 7.45 ml min^{-1} was observed. Literature often declares Pt as highly active for borohydride hydrolysis and Au as inert in respect thereof [23], other published ex-situ measurements contradict this statement [45,46]. The measurements for this thesis support the latter assumption that Au does not represent a faradaic efficient catalyst for BOR.

5.1 Outlook

A promising approach to face the borohydride hydrolysis reaction in DBFC could be the combination of the borohydride anion with organic cations leading to ionic liquids, for instance METMA BH_4 (2-methoxy-N,N,N-trimethylethan-ammonium borohydride) and DMMor BH4 – (4,4-dimetyl-morpholin-4-ium borohydride) instead of $NaBH_4$. Besides their application in the DBFC, ionic liquids can be used as efficient hydrogen storages.

6 References

[1] IPCC, Climate Change 2013: The Physical Science Basis. Summary for Policymakers, 2013.

[2] U. Cubasch, D. Wuebbles, D. Chen, M.C. Facchini, D. Frame, N. Mahowald, J.-G. Winther, Clim. Chang. 2013 Phys. Sci. Basis. Contrib. Work. Gr. I to Fifth Assess. Rep. Intergov. Panel Clim. Chang. (2013) 119–158.

[3] J. Larminie, A. Dicks, Fuel Cell Systems Explained, Second Edi, John Wiley & Sons, 2003.

[4] J. Töpler, Wasserstoff Und Brennstoffzelle, Springer Berlin Heidelberg, Berlin, Heidelberg, 2014.

[5] International Energy Agency, World Energy Outlook 2015, 2015.

[6] U.S. Department of Energy, (2016).

[7] U.B. Demirci, P. Miele, Energy Environ. Sci. 2 (2009) 627.

[8] Y. Okada, E. Sasaki, E. Watanabe, S. Hyodo, H. Nishijima, Int. J. Hydrogen Energy 31 (2006) 1348–1356.

[9] A.B. J.K. Ali, Appl. Catal. A Gen. 155 (1997) 41–57.

[10] U.S. Department of Energy, (2016).

[11] A.B. Stambouli, Renew. Sustain. Energy Rev. 15 (2011) 4507–4520.

[12] Y. Wang, K.S. Chen, J. Mishler, S.C. Cho, X.C. Adroher, Appl. Energy 88 (2011) 981–1007.

[13] P. Kurzweil, Brennstoffzellentechnik, 2013.

[14] European Commission, Hydrogen Energy and Fuel Cells, 2003.

[15] Fuel Cell Today, J. Matthey, (2013).

[16] G. Merle, M. Wessling, K. Nijmeijer, J. Memb. Sci. 377 (2011) 1–35.

[17] D.J.L. Brett, M. Manage, E. Agante, N.P. Brandon, E. Brightman, R.J.C. Brown, I. Staffell, Polym. Electrolyte Membr. Direct Methanol Fuel Cell Technol. (2012) 3–26.

[18] S. Weinberger, CHE.552, Fuel Cells Energy Storage (2015).

[19] A.D. McNaught, A. Wilkinson, IUPAC Compendium of Chemical Terminology (The "Gold Book"), 2014.

[20] B. Cornils, W.A. Herrmann, C. Wong, H. Zanthoff, R. Eds, Catalysis from A to Z, 2007.

[21] M.T.M. Koper, Y. Iwasawa, Phys. Chem. Chem. Phys. 16 (2014) 13567.

[22] F. Maillard, N. Job, M. Chatenet, Basics of PEMFC Including the Use of Carbon-Supported Nanoparticles, Elsevier B.V., 2013.

[23] E. Gyenge, Electrochim. Acta 49 (2004) 965–978.

[24] J. Ma, N. Choudhury, Y. Sahai, Renew. Sustain. Energy Rev. 14 (2010) 183–199.

[25] B.H. Liu, J.Q. Yang, Z.P. Li, Int. J. Hydrogen Energy 34 (2009) 9436–9443.

[26] U.B. Demirci, J. Power Sources 169 (2007) 239–246.

[27] I. Merino-Jiménez, C. Ponce De León, A.A. Shah, F.C. Walsh, J. Power Sources 219 (2012) 339–357.

[28] A. Aziznia, C.W. Oloman, E.L. Gyenge, J. Power Sources 212 (2012) 154–160.

[29] A. Serov, A. Aziznia, P.H. Benhangi, K. Artyushkova, P. Atanassov, E. Gyenge, J. Mater. Chem. A 1 (2013) 14384.

[30] C. Grimmer, R. Zacharias, M. Grandi, B. Pichler, I. Kaltenboeck, F. Gebetsroither, J. Wagner, B. Cermenek, S. Weinberger, A. Schenk, V. Hacker, J. Electrochem. Soc. 163 (2016) F278–F283.

[31] M.T. Reetz, M. Lopez, Method for In Situ Immobilization of Water-Soluble Nanodispersed Metal Oxide Colloids., WO2003078056, 2003.

[32] P.C. Favilla, J.J. Acosta, C.E. Schvezov, D.J. Sercovich, J.R. Collet-Lacoste, Chem. Eng. Sci. 101 (2013) 27–34.

[33] M. Chen, Y. Xing, Langmuir 21 (2005) 9334–9338.

[34] S.-A. Park, E.-K. Lee, H. Song, Y.-T. Kim, Sci. Rep. 5 (2015) 13552.

[35] Y. Wang, L. Cheng, F. Li, H. Xiong, Y. Xia, Chem. Mater. 19 (2007) 2095–2101.

[36] K.D. Vernon-Parry, III-Vs Rev. 13 (2000) 40–44.

[37] H.E. Swanson, R.K. Fuyat, G.M. Ugrinic, Standard X-Ray Diffraction Powder Patterns. IV. Data for 42 Inorganic Substances, 1955.

[38] P. Scherrer, Göttinger Nachrichten 2 (1918) 98.

[39] K.J.J. Mayrhofer, D. Strmcnik, B.B. Blizanac, V. Stamenkovic, M. Arenz, N.M. Markovic, Electrochim. Acta 53 (2008) 3181–3188.

[40] S. Treimer, A. Tang, D.C. Johnson, Electroanalysis 14 (2002) 165–171.

[41] A. Bard, L. Faulkner, Russ. J. Electrochem. 38 (2002) 1505–1506.

[42] K. Kordesch, S. Jahangir, M. Schautz, Electrochim. Acta 29 (1984) 1589–1596.

[43] C. Grimmer, S. Nestl, J. Senn, V. Hacker, Int. J. Hydrogen Energy 40 (2015) 2055–2061.

[44] C. Grimmer, R. Zacharias, M. Grandi, B. Cermenek, A. Schenk, S. Weinberger, F.A. Mautner, B. Bitschnau, V. Hacker, J. Phys. Chem. C 119 (2015) 23839–23844.

[45] M. Chatenet, F.H.B. Lima, E.A. Ticianelli, J. Electrochem. Soc. 157 (2010) B697–B704.

[46] F.H.B. Lima, A.M. Pasqualeti, M.B. Molina Concha, M. Chatenet, E.A. Ticianelli, Electrochim. Acta 84 (2012) 202–212.

[47] C. Grimmer, M. Grandi, R. Zacharias, B. Cermenek, H. Weber, C. Morais, T.W. Napporn, S. Weinberger, A. Schenk, V. Hacker, "Applied Catal. B, Environ. 180 (2016) 614–621.

[48] P. Piela, C. Eickes, E. Brosha, F. Garzon, P. Zelenay, J. Electrochem. Soc. 151 (2004) A2053.

[49] M. Lukaszewski, H. Siwek, A. Czerwinski, M. Łukaszewski, A. Czerwi, Electrochim. Acta 52 (2007) 4560–4565.

7 Appendix

7.1 Abbreviations

AFC	Alkaline fuel cell
BSE	backscattered electrons
BOR	Borohydride oxidation reaction
CE	Chemical reaction followed by electrochemical reaction
CV	Cyclovoltammetry
DBFC	Direct borohydride fuel cell
DMMor	4,4-dimetyl-morpholin-4-ium borohydride
DEMS	Differential electrochemical mass spectrometry
GDL	Gas diffusion layer
In-situ FTIR	In-situ Fourier transform infrared spectroscopy
METMA	2-methoxy-N,N,N- trimethylethan-ammonium borohydride
PAFC	Phosphoric acid fuel cell
PEMFC	Polymer electrolyte membrane fuel cell
PVP	Polyvinylpyrrolidone
RHE	Reversible hydrogen electrode
rpm	Revolutions per minute
SE	Secondary electrons
SHE	Standard hydrogen electrode
SOFC	Solid oxide fuel cell
TU	Thiourea

7.2 List of Figures